Dynamical Analysis of the Boundary Layer and Surface Wind Responses to Mesoscale SST Perturbations

LARRY W. O'NEILL

Marine Meteorology Division, Naval Research Laboratory, Monterey, California

STEVEN K. ESBENSEN, NICOLAI THUM, AND ROGER M. SAMELSON

College of Oceanic and Atmospheric Sciences, Oregon State University, Corvallis, Oregon

DUDLEY B. CHELTON

College of Oceanic and Atmospheric Sciences, and Cooperative Institute for Oceanographic Satellite Studies, Oregon State University, Corvallis, Oregon

ABSTRACT

The dynamical response of the marine atmospheric boundary layer (MABL) to mesoscale sea surface temperature (SST) perturbations is investigated over the Agulhas Return Current during winter from a 1-month, high-resolution, three-dimensional simulation using the Weather Research and Forecasting (WRF) mesoscale model. A steady lower boundary condition for July 2002 is obtained using SST measurements from the Advanced Microwave Scanning Radiometer on the Earth Observing System (EOS)–*Aqua* satellite (AMSR-E). The WRF models' ability to accurately simulate the SST-induced surface wind response is demonstrated from a comparison with satellite surface wind observations from the SeaWinds scatterometer on the Quick Scatterometer (QuikSCAT) satellite. Relevant features of this simulation include a quasi-periodic distribution of mesoscale SST perturbations with spatial scales ~200 km and strong winds that lead to a large surface sensible heat flux response, whose broad range of 80–100 W m^{-2} between warm and cool SST perturbations is much larger than seen in most previous simulations of mesoscale wind–SST coupling.

This simulation provides the first realistic example of vertical turbulent redistribution of momentum driven by the SST-induced surface heating perturbations acting in concert with the SST-induced pressure gradients to accelerate near-surface flow toward warm water and decelerate near-surface flow toward cool water. This simulation is also the first example of a near-surface wind speed response to mesoscale SST perturbations that differs qualitatively and substantially from the vertically averaged MABL wind response. In the vertically averaged MABL momentum budget, the surface wind stress acts as a drag on the SST-induced perturbation flow as it is being accelerated by SST-induced pressure gradients. However, only in the middle and upper reaches of the MABL does the turbulent stress divergence act as a drag on the SST-induced winds perturbations in this simulation.

These mesoscale SST perturbations are also shown to modify the wind direction within the MABL. Dynamically, this is accomplished through SST-induced perturbations to the crosswind components of the pressure gradient, turbulent stress divergence, and the Coriolis force.

1. Introduction

On spatial scales of 100–1000 km, satellite observations have consistently shown positive correlations between surface wind speed and mesoscale sea surface temperature (SST) variations (see reviews by Xie 2004; Chelton et al. 2004; Small et al. 2008). Small-scale features in the surface wind field generated by this ocean–atmosphere interaction are common near large midlatitude and equatorial ocean current systems and may have significant implications for underlying ocean circulations (Milliff et al. 1996; Spall 2007a; Seo et al. 2007; Jin et al. 2009; Hogg et al. 2009). The SST-induced

Corresponding author address: Larry W. O'Neill, Marine Meteorology Division, Naval Research Laboratory, 7 Grace Hopper Ave., MS#2, Monterey, CA 93943-5502.
E-mail: larry.oneill@nrlmry.navy.mil

Report Documentation Page

Form Approved
OMB No. 0704-0188

Public reporting burden for the collection of information is estimated to average 1 hour per response, including the time for reviewing instructions, searching existing data sources, gathering and maintaining the data needed, and completing and reviewing the collection of information. Send comments regarding this burden estimate or any other aspect of this collection of information, including suggestions for reducing this burden, to Washington Headquarters Services, Directorate for Information Operations and Reports, 1215 Jefferson Davis Highway, Suite 1204, Arlington VA 22202-4302. Respondents should be aware that notwithstanding any other provision of law, no person shall be subject to a penalty for failing to comply with a collection of information if it does not display a currently valid OMB control number.

1. REPORT DATE **31 JUL 2009**	2. REPORT TYPE	3. DATES COVERED **00-00-2009 to 00-00-2009**

4. TITLE AND SUBTITLE **Dynamical Analysis of the Boundary Layer and Surface Wind Responses to Mesoscale SST Perturbations**	5a. CONTRACT NUMBER
	5b. GRANT NUMBER
	5c. PROGRAM ELEMENT NUMBER
6. AUTHOR(S)	5d. PROJECT NUMBER
	5e. TASK NUMBER
	5f. WORK UNIT NUMBER
7. PERFORMING ORGANIZATION NAME(S) AND ADDRESS(ES) **Naval Research Laboratory,Marine Meteorology Division,Monterey,CA,93943**	8. PERFORMING ORGANIZATION REPORT NUMBER
9. SPONSORING/MONITORING AGENCY NAME(S) AND ADDRESS(ES)	10. SPONSOR/MONITOR'S ACRONYM(S)
	11. SPONSOR/MONITOR'S REPORT NUMBER(S)

12. DISTRIBUTION/AVAILABILITY STATEMENT
Approved for public release; distribution unlimited

13. SUPPLEMENTARY NOTES

14. ABSTRACT
see report

15. SUBJECT TERMS

16. SECURITY CLASSIFICATION OF:			17. LIMITATION OF ABSTRACT	18. NUMBER OF PAGES	19a. NAME OF RESPONSIBLE PERSON
a. REPORT **unclassified**	b. ABSTRACT **unclassified**	c. THIS PAGE **unclassified**	**Same as Report (SAR)**	**24**	

Standard Form 298 (Rev. 8-98)
Prescribed by ANSI Std Z39-18

adjustment of the marine atmospheric boundary layer (MABL) leads to surface winds that are stronger over warmer water and weaker over cooler water, a point well observed in satellite wind and SST fields (e.g., Xie et al. 1998; Rouault and Lutjeharms 2000; Liu et al. 2000; Chelton et al. 2001; Hashizume et al. 2001; Park and Cornillon 2002; Nonaka and Xie 2003; O'Neill et al. 2003; White and Annis 2003; Chelton et al. 2004; Vecchi et al. 2004; O'Neill et al. 2005; Tokinaga et al. 2005; Park et al. 2006; Chelton et al. 2007; O'Neill et al. 2010, 2009, manuscript submitted to *J. Climate*). This observed coupling between near-surface winds and mesoscale SST perturbations shows large geographical variability between the Northern and Southern Hemispheres and between the equatorial Pacific and extratropics. Less emphasized in most past studies is the effect of SST on the surface wind direction. Satellite scatterometer observations over the Gulf Stream have shown the surface winds rotate clockwise in flow from cool to warm water and rotate counterclockwise as winds blow the opposite way from warm to cool water (Park et al. 2006; Song et al. 2006). In O'Neill et al. (2009a), it is shown from Quick Scatterometer (QuikSCAT) surface wind observations that SST-induced wind directions variations are of this sense in the Northern Hemisphere and of the opposite sense in the Southern Hemisphere. Dynamical origins of the surface wind speed response to SST forcing have been investigated through observational, numerical, and analytical studies (as recently summarized in Small et al. 2008 and references therein). Few previous studies, however, have investigated the influence of mesoscale SST perturbations on wind direction.

The dynamical response of the MABL to mesoscale SST perturbations is examined here during July 2002 from a realistic, high-resolution, three-dimensional numerical simulation using the Weather Research and Forecasting (WRF) mesoscale model. This study is the first dynamical analysis of mesoscale wind–SST interactions in the extratropical Southern Ocean. Unique aspects of this region relevant for this simulation include: strong background winds between 10 and 16 m s^{-1} averaged over the 1-month simulation period; a much larger range of surface sensible heat flux perturbations of 80–100 W m^{-2} than seen in most previous model simulations; a quasi-periodic and quasi-stationary series of SST perturbations having a spatial scale of $O(200$ km) rather than a single SST front or ephemeral ocean eddies; a lack of complicating factors such as strong atmospheric stratification or capping inversions at the MABL top; and distance away from continental landmasses. These factors lead ultimately to a dynamical MABL response that differs substantially from previous simulations, as we will show in this analysis.

Two mechanisms have been identified in previous studies as fundamentally important in the MABL and surface wind response to mesoscale SST perturbations: generation of hydrostatic pressure gradients through adjustments of the MABL mass fields (e.g., Lindzen and Nigam 1987; Wai and Stage 1989; Warner et al. 1990; Small et al. 2003; Cronin et al. 2003; Bourras et al. 2004; Song et al. 2006) and stability-dependent modification of turbulent mixing of momentum from aloft to the surface (e.g., Sweet et al. 1981; Jury and Walker 1988; Wallace et al. 1989; Hayes et al. 1989; Wai and Stage 1989; Freihe et al. 1991; Jury 1994; Anderson 2001; Hashizume et al. 2002; de Szoeke and Bretherton 2004; Mahrt et al. 2004; Tokinaga et al. 2006; Skyllingstad et al. 2006). Over midlatitudes, horizontal advection and Coriolis accelerations also play prominent roles in the MABL wind response because of stronger westerly winds (e.g., Warner et al. 1990; Song et al. 2004; Bourras et al. 2004; Thum 2006; Song et al. 2006; Spall 2007b). Through these studies, mesoscale wind–SST coupling can be seen to vary with the spatial scale of the SST perturbations, the strength of the background wind, latitude, the presence of strong lower-tropospheric stratification and capping inversions, and proximity to landmasses.

In the conditions prevalent over the Agulhas Return Current region of interest here, the MABL is not in equilibrium with the mesoscale SST variations, leading to significant horizontal advection accelerations and an SST-induced response of the near-surface momentum budget that differs substantially from that of the vertically averaged momentum budget. Specifically, as expected, we will find that the surface wind stress acts as a drag on the perturbation pressure-driven flow when the MABL is considered as a whole. The model therefore reproduces the collocation of surface wind stress and SST perturbations seen in satellite wind and SST observations. As we will see in this simulation, however, the vertical turbulent redistribution of momentum acts in concert with SST-induced pressure gradients to accelerate or decelerate the near-surface winds. Only in the middle and upper portion of the MABL do the vertical turbulent stress divergence perturbations act as a drag on the SST-induced perturbation flow.

To understand the reason for these differences in the role of turbulent wind stress in the surface and vertically averaged momentum budgets, it is instructive to vertically integrate the turbulent stress divergence over the depth of the boundary layer H, which becomes $\int_0^H \partial \boldsymbol{\tau}/\partial z \, dz = \boldsymbol{\tau}_H - \boldsymbol{\tau}_s$, where $\boldsymbol{\tau}_H$ is the stress at the top of the boundary layer and $\boldsymbol{\tau}_s$ is the surface wind stress. For the purposes of this discussion, H is defined as the depth of the momentum boundary layer where the turbulent momentum flux $\boldsymbol{\tau}_H$ is much smaller than the

surface wind stress. The $\boldsymbol{\tau}_s$ boundary condition relative to a stationary surface is $\boldsymbol{\tau}_s = \rho C_d V^2$, where ρ is the surface air density, C_d is a stability-dependent drag coefficient, and V is the surface wind speed. Relative to a stationary surface, the surface wind stress will act as a drag on the vertically integrated boundary layer flow when driven by a pressure gradient that is relatively uniform with height since $\boldsymbol{\tau}_s$ is a positive quantity. The turbulent stress divergence $-\partial\boldsymbol{\tau}/\partial z$, however, is not necessarily proportional to the surface stress, or even of the same sign, since a simple turbulent exchange of momentum between the upper and lower part of the MABL will integrate to zero. This lack of a direct relationship between the surface wind stress and turbulent stress divergence at a given level within the MABL, while often overlooked, is pivotal for understanding how the surface wind stress can act as a drag on the MABL flow while turbulent stress divergence may accelerate or decelerate the near-surface winds.

Besides the SST-induced stability-dependent modification of the MABL turbulent stress divergence, mesoscale SST variations generate hydrostatic pressure gradients that can enter as a significant factor in the MABL momentum budget (e.g., Lindzen and Nigam 1987; Warner et al. 1990; Small et al. 2003; Bourras et al. 2004; Small et al. 2005; Song et al. 2006). Considering the MABL with depth $H = H_B + h$, where H_B is spatially constant and h is spatially varying, the horizontal hydrostatic pressure gradient ∇p at some height z within the MABL may be written as

$$\frac{1}{\rho_0}\nabla p(z) = -\frac{g}{\theta_0}\int_z^{H_B}\nabla\theta_v(z)\,dz + g'\nabla h + \frac{1}{\rho_0}\nabla p_T, \qquad (1)$$

where $\nabla\theta_v$ and ∇h are the horizontal virtual potential temperature and MABL depth gradients, respectively; ∇p_T is the horizontal pressure gradient just above the boundary layer top; θ_0 is a MABL reference potential temperature; ρ_0 is a MABL reference density; $g' = g\delta\theta/\theta_0$ is the reduced gravity; $\delta\theta$ is the potential temperature difference across the top of the MABL; and g is the gravitational constant. The first term in the rhs of Eq. (1) represents the influence of spatial air temperature gradients associated with mesoscale SST variations. These air temperature gradients have been shown to form as a balance between MABL temperature advection and surface sensible heat flux and tend to form downstream of SST gradients (Small et al. 2003). As is shown in the next section, pressure perturbations in this simulation result mainly from these SST-induced MABL air temperature perturbations. The second term in the rhs of Eq. (1) represents pressure gradient perturbations resulting from the deepening or shoaling of the MABL.

Hashizume et al. (2002) has shown over the eastern tropical Pacific that this term's contribution to the near-surface pressure gradient mostly negates the influence from the first term in what is sometimes called a "back pressure" effect; their observations showed that air temperature changes near the MABL top associated with SST-induced inversion height variations have opposite sign from those near the surface, and thus mostly cancel hydrostatic pressure changes associated with SST-induced air temperature changes near the surface. There is little indication that tropospheric pressure gradients [the third term on the rhs of Eq. (1)] are influenced significantly by mesoscale SST perturbations in this simulation.

To determine how SST-induced turbulent stress divergence and pressure gradient variations generate wind speed and direction variations within the MABL over this region of the Southern Ocean, we first obtain a high-resolution 1-month simulation using WRF. Details of the model simulation are presented in section 2, including the choice of realistic lateral and SST boundary conditions that allow comparison of the simulated WRF surface winds with satellite surface wind observations from the QuikSCAT scatterometer. In this section, we also describe some unique aspects of the SST and surface sensible heat fluxes relevant to this investigation. An analysis of the simulated MABL momentum budget is presented in section 3. We show that the momentum budget contains several features observed in previous simulations of mesoscale SST–wind coupling in other regions but also contains unique features not before seen. A straightforward dynamical explanation is presented to account for the MABL wind perturbations in this simulation consistent with the boundary layer vertically averaged momentum budgets and the vertical structure of the terms within the momentum budget.

2. Model simulation

a. Model description

The WRF atmospheric mesoscale modeling system (Skamarock et al. 2005) is utilized to simulate the MABL response to mesoscale SST perturbations over the Agulhas Return Current. WRF is the next generation of the widely used fifth-generation Pennsylvania State University–National Center for Atmospheric Research (PSU–NCAR) Mesoscale Model (MM5). The basic model configuration used for this simulation is briefly described here.

The model simulation was performed using a triple-nested configuration. The horizontal resolution of the outer nest was 75 km, the middle nest 25 km, and the inner nest was 8.3 km. The location of the inner nest is shown in Fig. 1 along with the SST field used in this
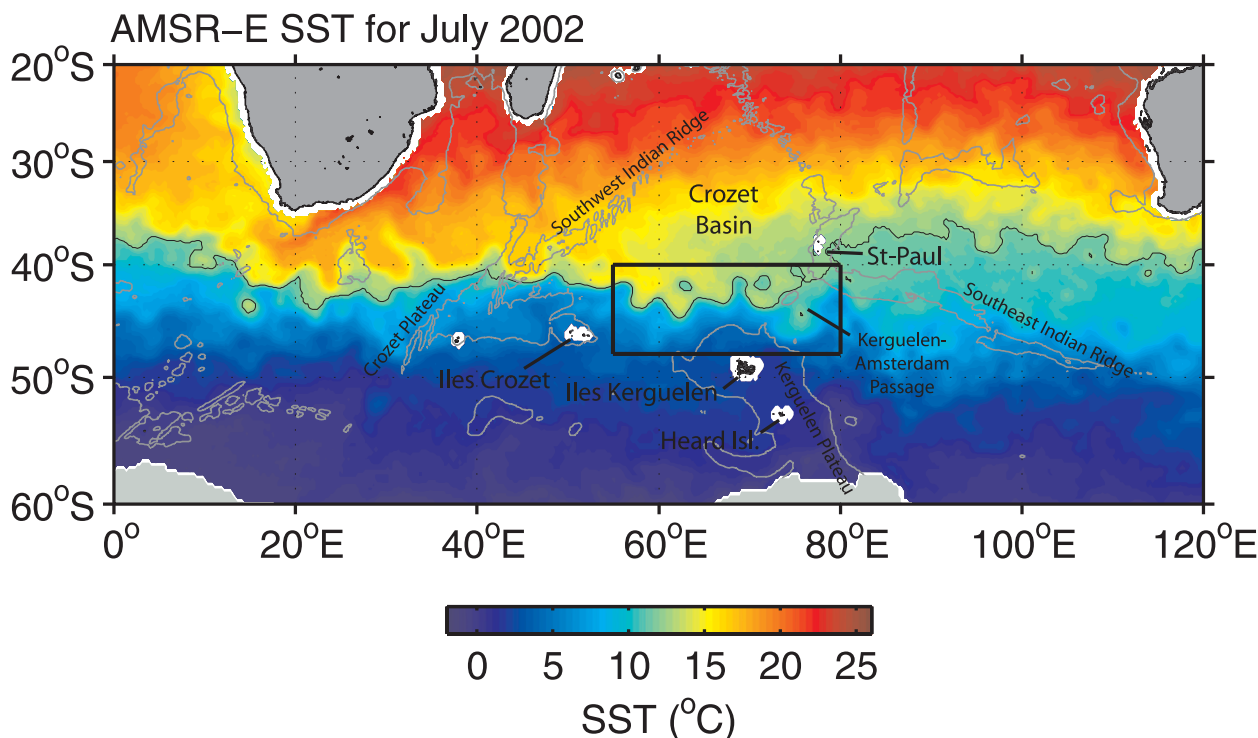
FIG. 1. Map of the AMSR-E SST over the Indian Ocean sector of the Southern Ocean averaged over July 2002. The area enclosed in the box is the location of the inner nest subject to the analysis in this paper. The thin black curve traces the 12°C SST isotherm. Gray contours mark the 3000-m isobath.

simulation, which is discussed further below. Only model fields from the inner fine-resolution nest are considered here. Along the lateral boundaries of the outer nest, the model dynamic and thermodynamic variables were updated every 6 h using the National Centers for Environmental Prediction (NCEP) operational analyses. During the 1-month period analyzed here, several large-scale transient weather disturbances that were initiated outside of the domain propagated through the domain. The NCEP time-dependent lateral boundary conditions thus enabled us to make a more realistic simulation for this time period to compare with the QuikSCAT wind observations. The simulation period is 1–31 July 2002, instantaneous model fields were output every 4 h, and only the fields after 2 July were used in this analysis (1-month averages here refer to the period 3–31 July).

The simulation was performed using a stretched vertical grid with 69 vertical levels, including 19 levels below 1000 m. The lowest level extends from the surface to 12-m height and the highest was near 20-km height. We chose a fine vertical resolution in the boundary layer to accurately resolve the vertical turbulent momentum exchange associated with the formation of convectively unstable and stable internal boundary layers.

The boundary layer parameterization implemented for this simulation was developed by Grenier and Bretherton (2001). This scheme is based on a 1.5-level turbulence closure method that includes detailed handling of moist MABL processes. The surface momentum flux was computed using a similarity-based boundary condition that uses a momentum roughness length from Charnock's relation to compute the surface friction velocity over the ocean. The surface layer scheme provides stability-dependent information for the boundary layer scheme, including surface exchange coefficients for heat, moisture, and momentum, but does not calculate any tendencies.

The ocean surface was assumed stationary for this analysis. Song et al. (2006) has shown that including the 1–2 m s^{-1} surface ocean current velocities associated with the Gulf Stream in the surface friction velocity computation made small but noticeable differences in the near-surface turbulent stress divergence. In this region of the Southern Ocean, however, surface ocean current velocities are only around 0.5–0.75 m s^{-1} within a small latitudinal band centered on 45°S latitude (e.g., Gille and Romero 2003; Lumpkin and Pazos 2007). We thus expect that inclusion of ocean current effects in the surface stress computations would lead only to minor differences from the simulation presented here.

The core of the WRF is the Advanced Research WRF (ARW) dynamic solver (Wang et al. 2004). This ARW solver provides the solutions to the fully compressible

nonhydrostatic equations on a mass-based terrain-following coordinate system and provides full two-way nesting capabilities, which were used here. Whenever possible, we have chosen options that have performed well in previous studies or are the defaults for the fifth-generation MM5 and NCEP–eta models. Microphysical parameterizations include explicitly resolved water vapor, cloud, and precipitation processes, and the WRF single-moment 3-class (WSM3) scheme was implemented. A modified version of the Kain–Fritsch scheme is used to represent subgrid-scale effects of convection and shallow clouds.

b. SST boundary condition and spatial filtering

For the SST boundary condition, we used a steady, 1-month-averaged SST field for July 2002 derived from SST observations made by the Advanced Microwave Scanning Radiometer on the Earth Observing System (EOS)–*Aqua* (AMSR-E) satellite (Fig. 1). Song et al. (2009) found that WRF simulations forced with the AMSR-E SST produced more accurate small-scale surface wind fields compared to those with the real-time global (RTG) SST or Reynolds SST analyses since the AMSR-E SST fields contains more realistic high-wavenumber SST variability. The month of July was chosen because the SST-induced surface wind stress response over the Agulhas Return Current is stronger during the austral winter than during the austral summer (O'Neill et al. 2005, 2009, manuscript submitted to *J. Climate*).

Removal of the large-scale SST field by spatial high-pass filtering reveals a rich array of SST perturbations corresponding to intrusions of water associated with the meandering Agulhas Return Current (Fig. 2b). Spatially high-pass-filtered fields were isolated in this study by removing spatially low-pass-filtered fields using a multidimensional loess smoothing function with half-power cutoff wavelengths of 10° latitude × 20° longitude (Schlax et al. 2001), similar to the smoothing characteristics of a 6° latitude × 12° longitude block-average smoother. Hereafter, fields spatially high-pass filtered in this manner are referred to as perturbation fields. The mesoscale SST perturbations thus obtained have a dynamic range of about ±4°C in the region of interest here (Fig. 2b).

A unique aspect of the SST field in this region is the quasi-periodic series of SST perturbations with wavelengths of roughly 200 km, well away from landmasses. Most previous modeling studies highlighted in the introduction have investigated flow over single SST fronts, such as flow perpendicular to the Gulf Stream or the cold tongue in the eastern equatorial Pacific, and not over such complicated SST features. As shown below, the response of the MABL is much different than in

these other studies and may be due to the rapid transitions the MABL undergoes when passing over these series of mesoscale warm and cool SST meanders.

To justify use of a steady SST field for this simulation, we quantified the temporal variability of the SST field over the Agulhas Return Current region using time-lagged autocorrelation functions of the unfiltered and perturbation AMSR-E SST fields. The autocorrelations were computed using 3-day-averaged SST fields at daily intervals centered on 14 July 2002 (Fig. 3a). The unfiltered AMSR-E SST has an autocorrelation function with a nearly constant value of 1 over time lags of ±15 days while the perturbation SST field has an autocorrelation function that falls off to about 0.75 at time lags of ±15 days. Both reveal that the SST field in this region evolves relatively slowly on submonthly time scales. Total SST differences during July 2002 are quantified using time-lagged RMS differences computed over all grid points in the SST field (Fig. 3b). Maximum RMS SST differences are about 1.1° and 0.8°C for the unfiltered and perturbation SST fields, respectively, some of which is due to the 0.4°C measurement uncertainties of individual AMSR-E SST observations (Chelton and Wentz 2005). Because SST features in this portion of the Agulhas Return Current are quasi-stationary during this period, we chose to use a steady 1-month SST field for simplicity in this WRF simulation.

The Kerguelen Plateau borders the southernmost part of the analysis region (Fig. 1). West of here, water enters into the Agulhas Return Current from the Agulhas Current and Agulhas Retroflection south of Africa near 40°S, 20°E. It then flows eastward, retaining its warm temperature and high-salinity characteristics until somewhere around 70°E (Lutjeharms and Ansorge 2001; Lutjeharms 2006), although this position is highly variable and has been observed to span anywhere between 60° and 80°E. Along its journey, water from the Agulhas Return Current slowly recirculates northward into the interior of the subtropical gyre in the southern Indian Ocean. East of the Kerguelen–Amsterdam Passage, the eastward flow loses its Agulhas water mass properties and is then called the South Indian Ocean Current (Belkin and Gordon 1996; Lutjeharms and Ansorge 2001). We will refer to this region as the Agulhas Return Current throughout this analysis despite the uncertainty over the exact location of its end position.

c. Simulated surface wind and pressure fields

The WRF model winds are strong during July 2002, with the 1-month scalar-averaged surface wind speeds increasing from about 10 m s^{-1} over the western portion of the domain to nearly 16 m s^{-1} over the southeastern portion (Fig. 2a). Westerly flow in the western portion of
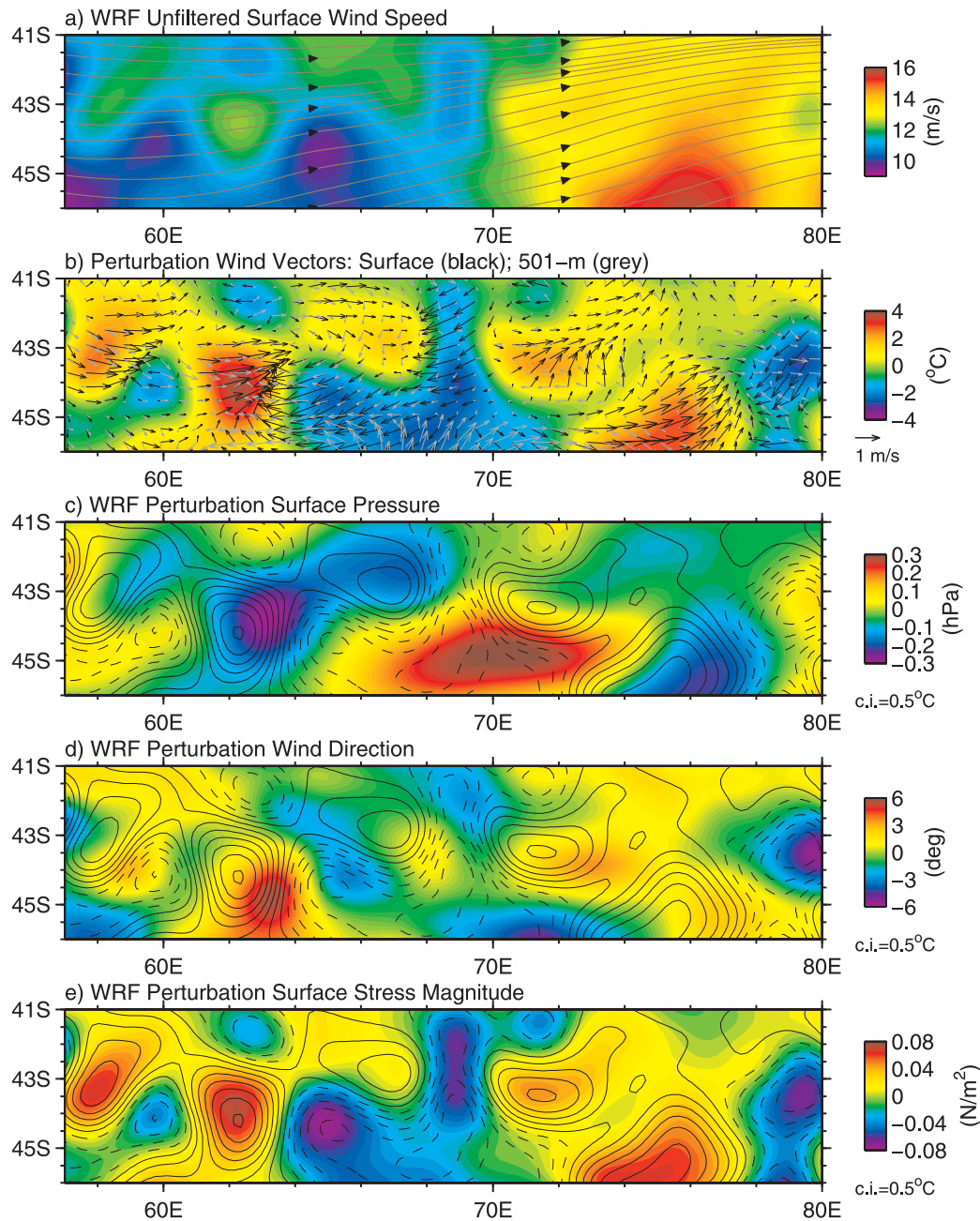
JOURNAL OF CLIMATE

FIG. 2. Maps of 1-month-averaged (a) WRF unfiltered scalar-averaged surface wind speed (colors) overlaid with streamlines of the WRF vector-averaged surface wind; (b) AMSR-E perturbation SST (colors) overlaid with vectors of the WRF vector-averaged perturbation surface wind (black) and wind at 501-m height (gray; for clarity, only every fourth vector is plotted); (c) WRF perturbation surface pressure (colors); (d) WRF perturbation surface wind direction (colors); (e) WRF perturbation surface wind stress magnitude (colors). The contours overlaid in (c)–(e) are of the AMSR-E perturbation SST having a contour interval (CI) of 0.5°C with solid and dashed contours corresponding to positive and negative values, respectively, and the zero contour has been omitted for clarity. A reference vector key is located below the color bar in (b).

the domain progressively becomes more southwesterly toward the east, as evident by the southwest to northeast tilt of streamlines computed from the 1-month vector-averaged WRF surface wind (Fig. 2a). Although difficult to see in these streamlines, the surface winds turn northward downwind of warm SST and southward downwind of cool SST, as evident from the perturbation surface wind vectors shown in Fig. 2b and the perturbation
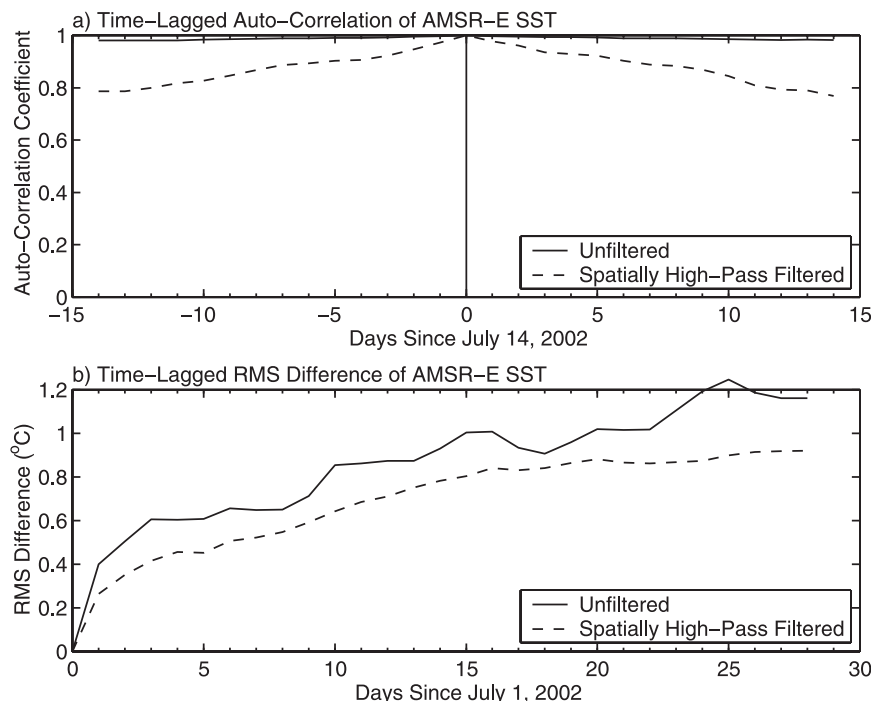
FIG. 3. (a) Time-lagged autocorrelation functions for the AMSR-E unfiltered SST (solid line) and spatially high-pass-filtered SST (dashed line) computed for 14 Jul 2002. (b) Time-lagged RMS differences between the AMSR-E SST field on 1 Jul 2002 and the SST fields lagged in time afterward. The statistics in both panels were computed from 3-day-averaged AMSR-E SST fields at daily intervals over the region 50°–40°S, 50°–80°E.

wind direction shown in Fig. 2d. This is quantified statistically by histograms of the perturbation wind direction separated by warm and cool SST perturbations (Fig. 4a). These wind direction perturbations give rise to a turning of the westerly winds in this region and will be discussed further below. Similar SST-induced wind direction changes have been shown to varying degrees in numerical model simulations and observations (e.g., Park et al. 2006; Song et al. 2006; Spall 2007b; O'Neill

et al. 2010). Likewise, the surface wind speed perturbations are, on average, positive over warm SST and negative over cool SST (Fig. 4b). The perturbation wind vectors aloft at 501-m height are also shown in Fig. 2b. Note that the perturbation flow aloft is much different than near the surface. The vertical structure of the wind is discussed in greater detail in section 3.

Simulated mesoscale surface wind speed perturbations coincide closely with the mesoscale SST perturbations
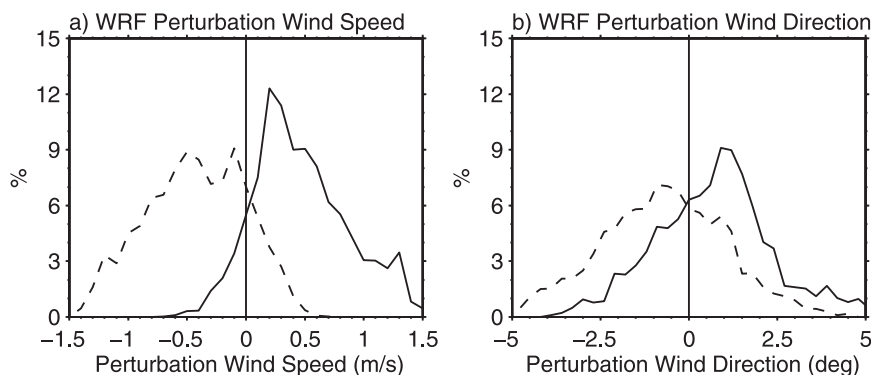

FIG. 4. Histograms of the WRF 1-month scalar-averaged perturbation (a) surface wind speed and (b) surface wind direction separated between positive (solid curves) and negative (dashed curves) perturbation SSTs.
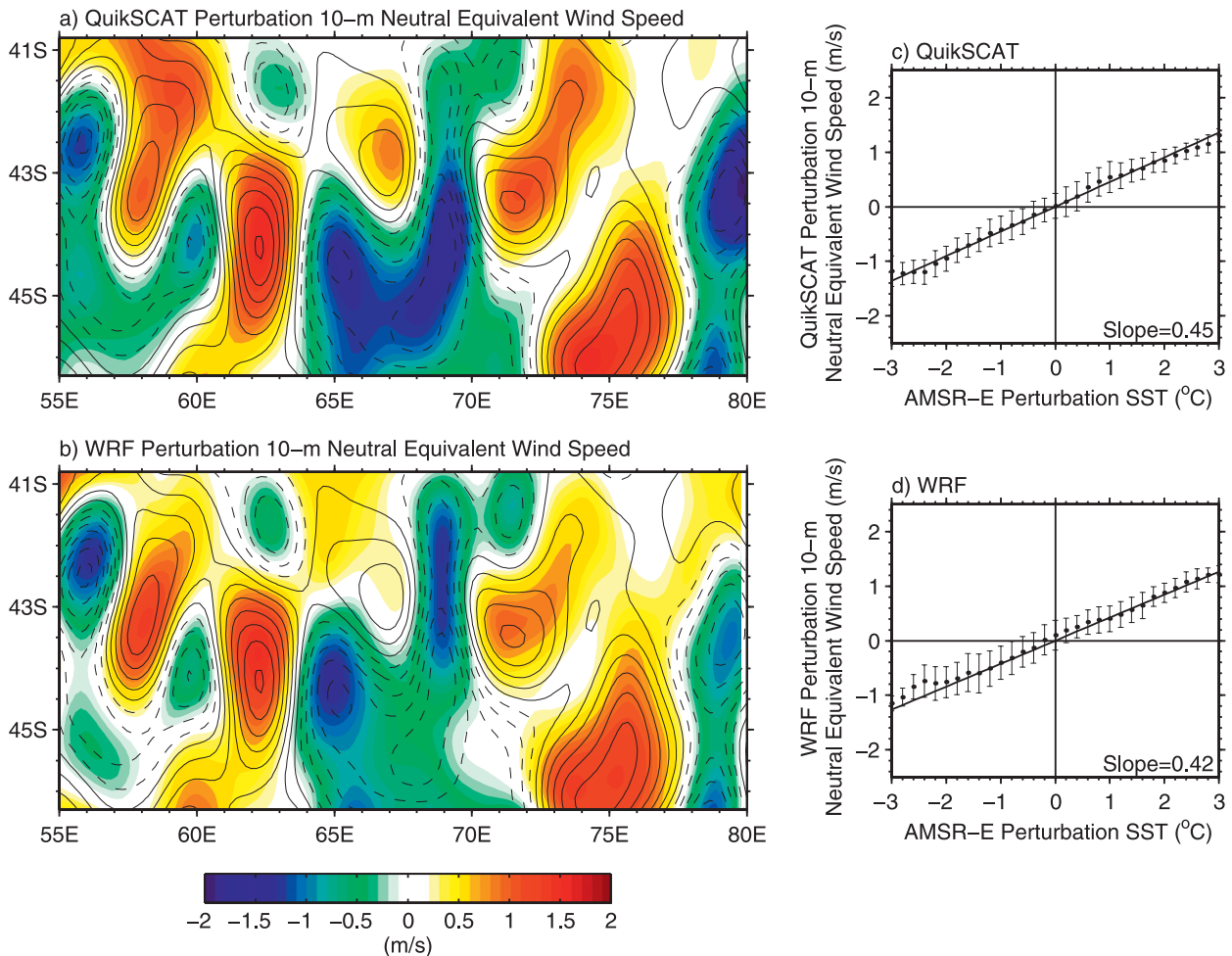
FIG. 5. (left) Maps of 1-month scalar-averaged perturbation 10-m equivalent neutral stability wind speed (colors) from (a) QuikSCAT and (b) WRF during July 2002. The solid and dashed contours correspond to positive and negative AMSR-E SST perturbations, respectively, with a CI of 0.5°C; the zero contour has been omitted for clarity. (right) Binned scatterplots of 1-month-averaged perturbations of the scalar 10-m equivalent neutral stability wind speed as a function of the AMSR-E SST for (c) QuikSCAT and (d) WRF. The regression lines in (c) and (d) are linear least squares fits of the points having a slope as indicated at the lower right, and the error bars represent ±1 std dev of the perturbation wind speeds within each bin.

(Fig. 5b), with increased wind speed over warm SST and decreased wind speed over cool SST. The surface wind stress magnitude perturbations are also similarly affected (Fig. 2e). To evaluate the ability of WRF to simulate these SST-induced surface wind speed perturbations, we compute the 1-month scalar-averaged 10-m equivalent neutral stability wind speed (Liu and Tang 1996) from WRF and compare them with that observed from the QuikSCAT scatterometer (Figs. 5a,b). These maps show qualitatively that the WRF simulation accurately portrays the relative locations and magnitudes of the SST-induced surface wind perturbations. This is quantified statistically from binned scatterplots of the 10-m equivalent neutral stability wind speed as a function of the AMSR-E perturbation from WRF and QuikSCAT

(Figs. 5c,d). The perturbation wind speed V' is related linearly to the perturbation SST T' in both the WRF and QuikSCAT and can be expressed as

$$V' = \alpha_0 T'. \qquad (2)$$

The slope α_0 computed from the WRF simulation is within about 10% of that computed from the QuikSCAT observations. The close quantitative correspondence between the SST-induced surface wind speed response simulated by WRF and observed by QuikSCAT gives confidence in the WRF model's ability to accurately simulate the momentum budget associated with the SST-induced perturbation surface wind.

Low pressure perturbations form about 100–200 km downwind of warm SST perturbations while high pressure

perturbations form about the same distance downwind of cool SST perturbations (Fig. 2c). The range of these SST-induced surface pressure perturbations is about ±0.25 hPa, which is comparable to, if not somewhat larger than, those found in previous observational and modeling studies (e.g., Wai and Stage 1989; Warner et al. 1990; Cronin et al. 2003; Small et al. 2003, 2005; Song et al. 2006). Perturbations in the model surface pressure field form hydrostatically as a result of a balance between surface heating and boundary layer temperature advection in the thermodynamic energy equation (Small et al. 2003). Consistent with this balance, θ_v perturbations vertically integrated between the surface and 1205-m height are located downwind of the SST perturbations (Fig. 6a). As shown by the first term in Eq. (1), surface pressure perturbations are associated closely with these SST-induced perturbations in the vertically integrated θ_v field, as evident from Fig. 6b; the cross-correlation coefficient between these surface pressure and vertically integrated θ_v fields is −0.87. According to Eq. (1), a vertically integrated θ_v perturbation of 600°C·m and $\theta_0 = 285$ K yields a surface pressure perturbation of about 0.21 hPa, which agrees well with these surface pressure perturbations.

As pointed out previously, SST-induced surface heating drives modification of the MABL mass and turbulence fields. The WRF surface sensible heat flux perturbations are shown in Fig. 6c and are enhanced by warm SST and reduced by cool SST, consistent with previous studies. The difference between warm and cool SST in this simulation is about 80–100 W m^{-2}, or roughly 15 W m^{-2} (°C SST)$^{-1}$ change, which is a range significantly larger than reported in most previous modeling studies over other regions (e.g., Small et al. 2003; Song et al. 2004; Bourras et al. 2004; de Szoeke and Bretherton 2004; Small et al. 2005; Seo et al. 2007) but comparable to the simulation of Wai and Stage (1989). Since there is no significant capping inversion at the MABL top to reduce the surface pressure signal (the back-pressure effect; Hashizume et al. 2002), the larger sensible heat flux perturbations are likely responsible for the stronger surface pressure perturbations seen in this simulation. It is unclear what role ocean dynamics play in maintaining these strong heat fluxes in the real ocean.

We conclude this section by noting that Liu et al. (2007) has suggested that SST-induced surface wind speed perturbations are driven mainly by stability-dependent changes to the logarithmic wind profile in the surface layer (i.e., Stull 1988, p. 377). To test whether this mechanism can account for the surface wind speed perturbations in this simulation, we computed the difference between perturbations of the 10-m stability-dependent wind speed and the 10-m equivalent neutral

stability wind speed (Fig. 6d). In unstable conditions over warm SST, the stability-dependent wind speed is about 0.2 m s^{-1} less than in neutral conditions, as expected, with the opposite occurring in more stable conditions over cool SST. This can only account for less than 15% of the value of the surface wind speed perturbations found in this simulation, however, and thus cannot fully explain the SST-induced surface wind speed response. As shown in the next section, SST-induced surface stress variations in this simulation are due to SST-induced pressure gradients, turbulent momentum redistribution, and horizontal advection rather than to changes in surface layer stability. This is consistent with several previous investigations of surface layer stability effects associated with mesoscale SST perturbations (Wai and Stage 1989; Small et al. 2003; O'Neill et al. 2005; Spall 2007b; Song et al. 2009; O'Neill et al. 2009, manuscript submitted to *J. Climate*).

3. Momentum budget analysis

The momentum budget analyzed here has been rotated into local downwind and crosswind components using natural coordinates, where the downwind momentum budget describes the evolution of wind speed while the crosswind direction describes the evolution of wind direction. One main advantage of analyzing the MABL momentum budget in natural coordinates is that the forcing terms do not depend on the ambient large-scale wind direction, which is important here since the large-scale flow is not aligned uniformly along the fixed model coordinates and the flow direction varies significantly on hourly time scales. Dominant terms in the WRF perturbation downwind and crosswind momentum budget, respectively, are

$$\left(V\frac{\partial V}{\partial s}\right)' = \left(-w\frac{\partial V}{\partial z} - \frac{1}{\rho}\frac{\partial p}{\partial s} + \mathbf{F}\cdot\hat{s}\right)', \qquad (3)$$

$$\left(V^2\frac{\partial \psi}{\partial s}\right)' = \left(-wV\frac{\partial \psi}{\partial z} - fV - \frac{1}{\rho}\frac{\partial p}{\partial n} + \mathbf{F}\cdot\hat{n}\right)', \qquad (4)$$

where (s, n, z) are the local downwind, crosswind, and vertical spatial coordinates, respectively; V is the wind speed; ψ is the counterclockwise wind direction relative to the fixed eastward direction; $w = dz/dt$ is the vertical velocity; f is the Coriolis parameter; ρ is the air density; p is the air pressure; $\mathbf{F}\cdot\hat{s}$ and $\mathbf{F}\cdot\hat{n}$ are, respectively, the downwind and crosswind components of the Reynolds vertical turbulent stress divergence $\mathbf{F} = (F^x, F^y) = (1/\rho)(\partial/\partial z)(\tau^x, \tau^y)$; $\tau^x = -\rho\overline{u'w'}$ and $\tau^y = -\rho\overline{v'w'}$ are the subgrid-scale Reynolds stresses in the zonal and
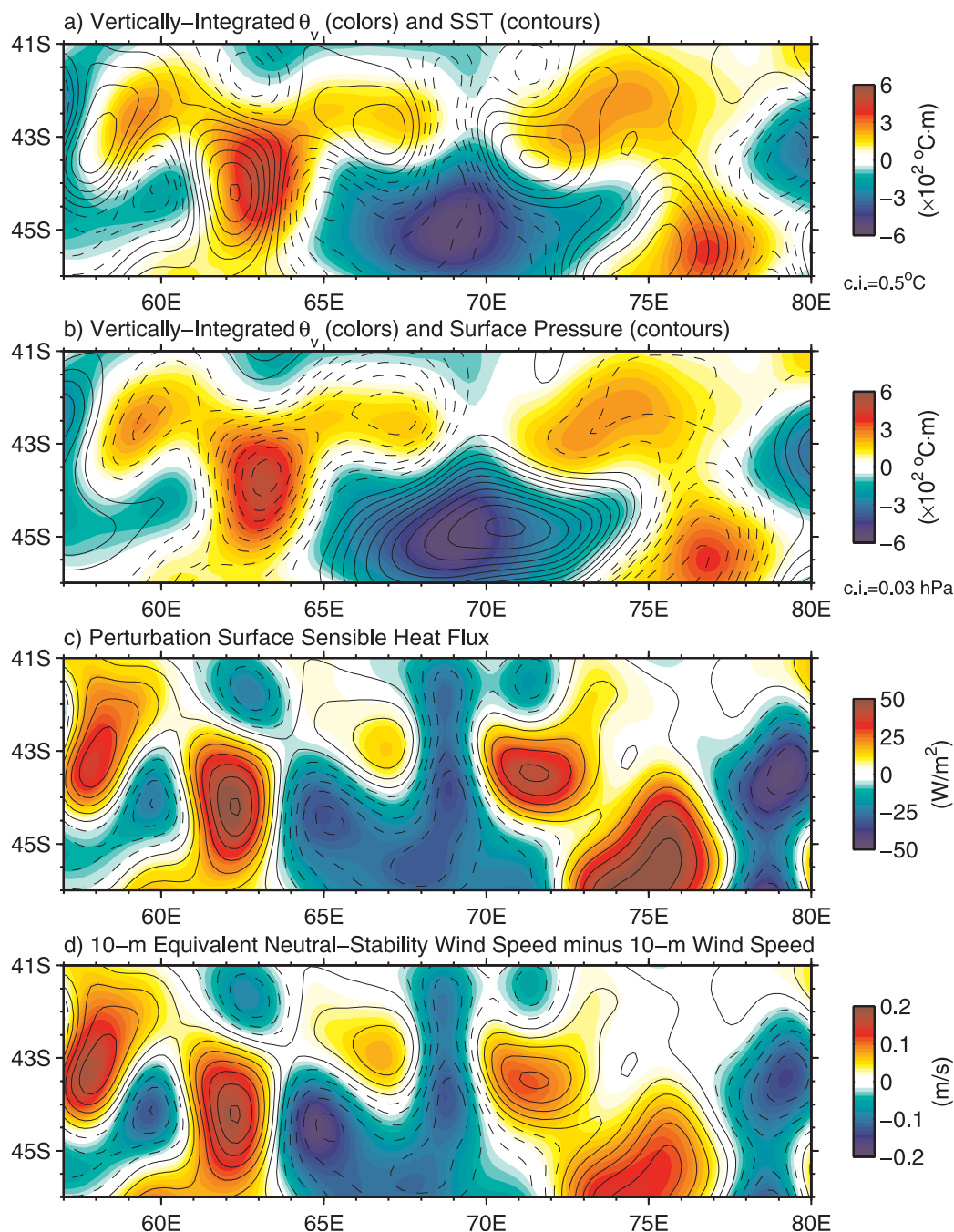
FIG. 6. Maps averaged over the 1-month period of the WRF simulation: (a) perturbation vertically integrated virtual potential temperature; (b) perturbation vertically integrated virtual potential temperature overlaid with contours of perturbation surface pressure; (c) perturbation surface sensible heat flux; (d) perturbation 10-m equivalent neutral stability wind speed minus the perturbation 10-m stability-dependent wind speed, both from WRF. Contours in (a),(c), and (d) are of the AMSR-E perturbation SST shown earlier.

meridional directions, respectively; $(\hat{s}, \hat{n})$ are unit downwind and crosswind vectors, respectively; $-(1/\rho)(\partial p/\partial s)$ and $-(1/\rho)(\partial p/\partial n)$ represent the downwind and crosswind pressure gradient, respectively; and $w\partial V/\partial z$ and $wV\partial\psi/\partial z$ represent the downwind and crosswind verti-

cal advection, respectively. The local acceleration and horizontal components of the Reynolds-averaged terms not shown in Eqs. (3) and (4) are comparatively small when averaged over the 1-month period analyzed here. Since the local acceleration term is negligible, the downwind

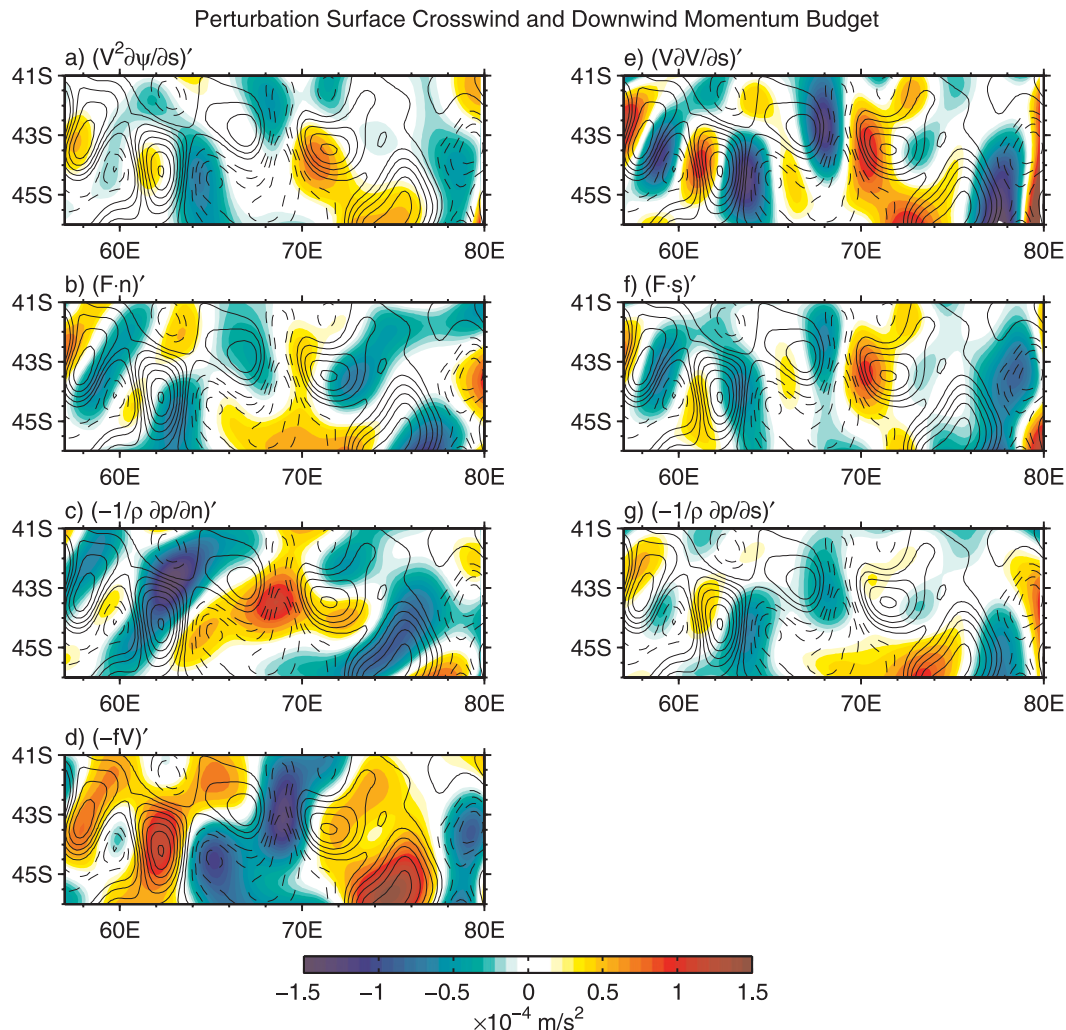Perturbation Surface Crosswind and Downwind Momentum Budget

FIG. 7. Maps of the 1-month-averaged perturbation terms of the WRF surface momentum budget: horizontal advection in the (a) crosswind and (e) downwind directions; turbulent stress divergence in the (b) crosswind and (f) downwind directions; pressure gradient in the (c) crosswind and (g) downwind directions; (d) Coriolis force. The dashed and solid contours in each panel correspond to negative and positive AMSR-E SST perturbations, respectively, with a CI of 0.5°C. The zero contour has been omitted for clarity.

and crosswind horizontal advective tendencies in these equations ($V\partial V/\partial s$ and $V^2\partial\psi/\partial s$, respectively) interchangeably describe along- and cross-streamline air parcel accelerations, respectively. Crosswind horizontal advection is also known as centrifugal acceleration V^2/R, where $R^{-1} = \partial\psi/\partial s$ is the local radius of streamline curvature.

a. Surface momentum budget

1) SURFACE DOWNWIND MOMENTUM BUDGET

Perturbations in both the downwind turbulent stress divergence and downwind pressure gradient are comparable in magnitude and act in concert to increase the surface wind speed toward warm SST and decrease the surface wind speed toward cool SST (Figs. 7e–g). In this simulation, both turbulent momentum mixing and pressure gradients are thus important in the SST-induced surface wind speed response. Other examples of these two mechanisms acting together over mesoscale SST perturbations are not readily apparent from previous model simulations; one mechanism has usually been shown to dominate over the other. Near the surface, this result may be interpreted as a mixture of the Wallace et al. (1989) and Hayes et al. (1989) turbulent mixing mechanism and the Lindzen and Nigam (1987) and Small et al. (2005) surface pressure gradient forcing mechanism. Note that the surface downwind turbulent stress divergence perturbations are not collocated spatially with the surface stress perturbations (Fig. 2e).

This balance differs from the simulation of Small et al. (2005) for cross-equatorial surface flow over the equatorial Pacific. In that simulation, the surface turbulent stress divergence was seen to act as a drag on the perturbation flow driven by SST-induced surface pressure gradients until they balanced some distance downwind of the northern cold tongue SST front. We show in section 3b that the Small et al. (2005) "pressure–drag" balance does hold above about 150 m in this simulation, but not down to the surface.

Modulation of near-surface winds by SST-induced turbulent mixing has also been seen in simulations by de Szoeke and Bretherton (2004) over the eastern tropical Pacific and Skyllingstad et al. (2006) for an idealized case study of smaller-scale SST fronts with length scales of $O(10$ km$)$. In both these studies, however, SST-induced surface pressure gradients were found to have much less influence than found here. Effects of SST-induced pressure gradients on the surface winds are consistent with several other modeling studies (Wai and Stage 1989; Warner et al. 1990; Small et al. 2003, 2005; Song et al. 2006).

Using an idealized two-dimensional coupled simulation characteristic of a midlatitude SST front, Spall (2007b) found that cross-frontal surface wind changes away from the frontal region were consistent with the one-dimensional balance proposed by Samelson et al. (2006), where changes in surface drag, compensating for cross-frontal changes in boundary layer height, caused a change in cross-frontal wind strength at the expense of the along-frontal winds via the Coriolis force. SST-induced pressure gradients and turbulent mixing were insufficient to account for the cross-frontal wind changes, which differ on both accounts from this simulation.

In its simplest form, the Samelson et al. (2006) hypothesis assumes that the ratio of surface stress to boundary layer depth remains constant for a given vertically uniform background pressure gradient. The applicability of the Samelson et al. (2006) quasi-equilibrium adjustment mechanism for this region can be tested by computing a ratio of the surface drag time scale T_τ and the advective time scale T_A:

$$\gamma_{\tau A} = \frac{T_\tau}{T_A} = \frac{H_B V \Delta V}{\tau L},$$

where H_B, V, ΔV, τ, and L are characteristic values of, respectively, MABL depth, wind speed, cross-frontal wind speed change, wind stress, and frontal length scale. For typical values in this region of $H_B = 1000$ m, $V = 12$ m s^{-1}, $\Delta V = 3$ m s^{-1}, $\tau = 0.15$ N m^{-2}, and $L = 200$ km, then $\gamma_{\tau A} = 1.2$, and the quasi-equilibrium as-

sumption for this region is tenuous. This is consistent with the simulations presented here, where the nonequilibrium effects of SST-induced pressure gradients, turbulent mixing, and horizontal advection dominate the surface momentum budget response. The part of the perturbation surface stress that balances the perturbation downwind pressure gradient and horizontal advection in this simulation is considered separate from the hypothesis of Samelson et al. (2006).

2) SURFACE CROSSWIND MOMENTUM BUDGET

In addition to the waxing and waning of surface wind speed as air flows over these mesoscale SST perturbations, surface winds turn counterclockwise in flow toward warm SST and clockwise in flow toward cool SST, as shown by the perturbation wind direction in Fig. 2d and the crosswind advection perturbations in Fig. 7a. Coriolis force and crosswind pressure gradient perturbations are the largest terms in the surface crosswind momentum budget (Figs. 7c,d), although the crosswind turbulent stress divergence is a significant contributor (Fig. 7b). The imbalance between these three forces results in significant curvature perturbations over the strongest downwind SST gradients.

Coriolis force perturbations result from SST-induced wind speed perturbations (Fig. 7d) and are thus highly correlated with the SST perturbations and are significant even on the small scale of these SST perturbations. The length scale over which the Coriolis term can change the wind direction in inertial flow is Vf^{-1}, and for $V = 12$ m s^{-1} this implies a radius of curvature of 120 km, which is smaller than the $\sim$200-km length scale of the SST perturbations in this region. Note, however, that pure inertial flow is not achieved here on the mesoscale in this simulation since the SST-induced crosswind pressure gradients and crosswind turbulent stress divergence perturbations are large. Additionally, the crosswind pressure gradient and turbulent stress divergence perturbations are not collocated with the Coriolis force perturbations. The crosswind pressure gradient and Coriolis force perturbations are of the same sign on the southeastern (northwestern) flanks of warm (cool) SST and of opposite sign on the northwestern (southeastern) flanks of warm (cool) SST. Crosswind turbulent stress divergence perturbations tend to form in regions where the downwind SST gradients are strongest and contribute to a turning of the winds that are anticyclonic in flow from cool to warm SST and cyclonic in flow from warm to cool SST. This behavior does not appear to be noted in other simulations. As discussed in the next section, SST-induced crosswind turbulent stress perturbations are consistent with a thermal wind adjustment of the crosswind vertical wind shear.

Significant Coriolis accelerations were also found in the simulations of Song et al. (2006) and Spall (2007b). The model simulations used by Wai and Stage (1989) and Spall (2007b) had fixed along-frontal pressure gradients and therefore SST-induced crosswind pressure gradients could not develop. In the Song et al. (2006) simulation, crosswind pressure gradients did partially balance the Coriolis force, consistent with this simulation. The near-equatorial simulations by Small et al. (2003, 2005) had little influence from the Coriolis force, and it appears that the pressure gradient and turbulent stress divergence in the crosswind direction opposed each other analogous to the downwind balance.

b. Response of the MABL vertical structure to mesoscale SST perturbations

1) ANALYSIS METHOD

Physical mechanisms for the three-dimensional response of the 1-month average forcing terms in Eqs. (3) and (4) are efficiently and unambiguously separated here using empirical orthogonal functions (EOFs). An arbitrary field $d(x, y, z)$ is decomposed into a set of M horizontal spatial modes $G_k^d(x, y)$ and amplitude vertical profiles $a_k^d(z)$ such that

$$d(x, y, z) = \sum_{k=1}^{M} a_k^d(z) G_k^d(x, y).$$

These EOFs are analogous to those computed from a set of time series at discrete spatial grid locations except that $a_k^d(z)$ represents amplitude vertical profiles for each mode k instead of amplitude time series. Use of EOFs in this way allows quantitative analysis of the coherent vertical and horizontal responses of the MABL forcing terms to mesoscale SST perturbations. The EOFs were computed using singular value decomposition without removing the vertical mean at each grid location. The set of eigenvectors $G_k^d(x, y)$ were normalized to 1 and the amplitude vertical profiles $a_k^d(z)$ were multiplied by the corresponding normalization factor.

EOFs are conventionally computed with the mean removed at each grid point to express vertical variability with respect to the vertical mean. For this analysis, the vertical variability associated with the vertical mean is of particular interest, and thus the vertical mean is not removed before computing the EOFs. As a result, instead of explaining vertical variance as in the case when the vertical mean is removed, the EOFs here explain the vertical ''mean product.'' For all perturbation terms considered, the first two modes explain better than 80% of each terms' total vertical mean product; we therefore only consider the first two modes of each term.

To evaluate this EOF representation of the 1-month average forcing terms, we compare vertical profiles of the terms in the downwind momentum budget (excluding vertical advection) and the Coriolis force with the sum of the first two EOF modes for each term (Fig. 8). Three locations are chosen to represent different flow regimes: one where flow is from cool to warm SST (44.5°S, 61°E), one where flow is from warm to cool SST (42.2°S, 68°E), and one at a perturbation SST minimum (44°S, 65°E). Except for some minor differences, the EOFs capture most of the important vertical structure of these forcing terms. As we shall see next, these EOFs prove powerful for isolating the physical processes determining the vertical structure of the perturbation forcing terms.

2) WIND SPEED AND THE DOWNWIND MOMENTUM BUDGET

The first horizontal spatial mode of the perturbation wind speed ($G_1^{V'}$) shown in Fig. 9 is well correlated with the SST perturbations. Its corresponding amplitude vertical profile ($a_1^{V'}$) indicates that SST mostly affects the perturbation wind speed below 800 m. This coherent variability accounts for 76.6% of the vertical variability of the perturbation wind speed. The first two EOFs of the perturbation downwind horizontal advection (Fig. 10) have amplitude vertical profiles that are related closely to the amplitude vertical profiles of the first two EOFs of the perturbation wind speed (Fig. 9).

The first EOF of the downwind turbulent stress divergence has minimal effect at the surface (Fig. 10). Its second EOF shows strong intensification below 150-m height and has a spatial mode $G_2^{(\mathbf{F} \cdot \hat{s})'}$ corresponding closely to the surface map of $(\mathbf{F} \cdot \hat{s})'$ shown in Fig. 7f. The cross-correlation coefficient between $G_2^{(\mathbf{F} \cdot \hat{s})'}$ and $(\mathbf{F} \cdot \hat{s})'$ at the surface is 0.92. Below 150 m, SST-induced turbulent mixing acts to accelerate the winds when the flow is from cool to warm SST and decelerate the winds when the flow is from warm to cool SST, which is nearly identical to what occurs at the surface (Fig. 7f). This profile is consistent with the formation of internal boundary layers at the upwind edges of the SST fronts (e.g., Mahrt et al. 2004; Song et al. 2004; Skyllingstad et al. 2006; Thum 2006). The vertical profile $a_2^{(\mathbf{F} \cdot \hat{s})'}$ becomes slightly negative above 150 m to about 900 m, consistent with turbulence exchanging momentum between the upper and lower MABL. The effect of $a_2^{(\mathbf{F} \cdot \hat{s})'}$ on the surface stress can be estimated by vertically integrating $a_2^{(\mathbf{F} \cdot \hat{s})'}$ from the surface to $H_B = 1205$ m, yielding $\int_0^{H_B} \rho_0 a_2^{(\mathbf{F} \cdot \hat{s})'}(z) \, dz = -0.004$ N m^{-2}, which is much smaller than the surface stress perturbations of ~ 0.1 N m^{-2} (Fig. 2e). In this simulation, turbulent redistribution of momentum can thus lead to significant near-surface wind speed changes associated
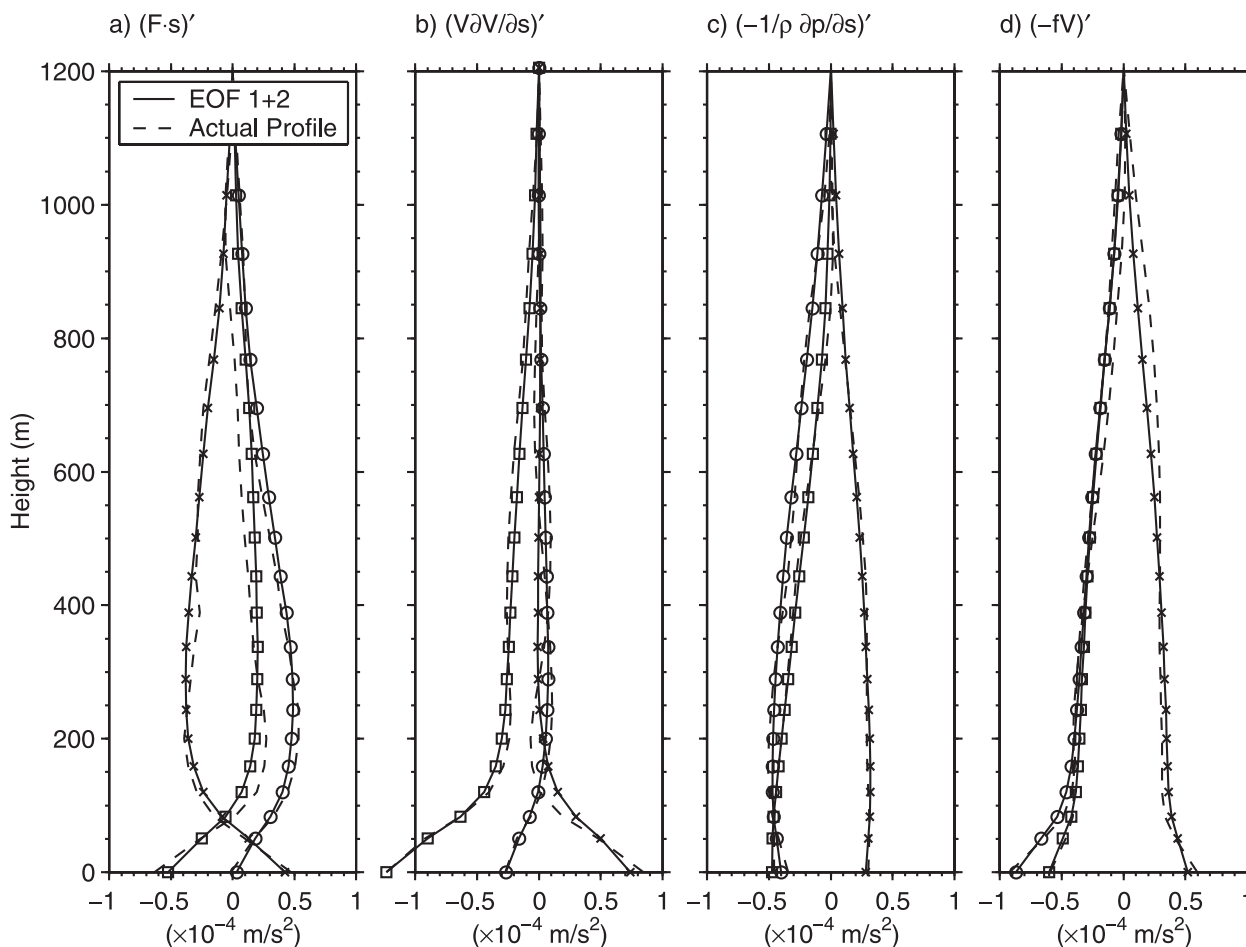
FIG. 8. Vertical profiles of select 1-month-averaged forcing terms in the WRF momentum budget at three different points (dashed) along with the EOF representation of these terms computed from the first two modes (solid). Four terms are chosen: (a) downwind turbulent stress divergence $(\mathbf{F} \cdot \hat{s})'$; (b) downwind horizontal advection $(V\partial V/\partial s)'$; (c) downwind pressure gradient $[-(1/\rho)(\partial p/\partial s)]'$; (d) Coriolis force $(-fV)'$. The three locations chosen are 44°S, 61°E (crosses; cool to warm); 44.5°S, 65°E (circles; SST minimum); and 42.2°S, 68°E (squares; warm to cool).

with the mesoscale SST perturbations while having little affect on the surface stress. As shown in section 3c, downwind surface stress perturbations balance the perturbation downwind pressure gradient vertically averaged over the depth of the MABL, consistent with the Small et al. (2005) pressure–drag balance.

The first EOFs of the downwind turbulent stress divergence and downwind pressure gradient, on the other hand, show just the opposite above 150-m height: the $G_1^{(\mathbf{F}\cdot\hat{s})'}$ and $G_1^{[-(1/\rho)(\partial p/\partial s)]'}$ fields are negatively correlated, resulting in the turbulent stress divergence opposing the downwind pressure gradient and thus acting as a drag on the perturbation flow driven by the SST-induced pressure gradients. The cross-correlation coefficient between $G_1^{(\mathbf{F}\cdot\hat{s})'}$ and $G_1^{[-(1/\rho)(\partial p/\partial s)]'}$ is -0.85 when the downwind turbulent stress divergence perturbations are lagged 45 km downwind of the downwind pressure gradient

perturbations. Below 150-m height, $a_1^{(\mathbf{F}\cdot\hat{s})'}$ diminishes rapidly relative to $a_1^{[-(1/\rho)(\partial p/\partial s)]'}$ and is nearly zero at the surface and thus cannot explain the balance at the surface seen in Fig. 7. Above 150 m, the downwind shift of $G_1^{(\mathbf{F}\cdot\hat{s})'}$ relative to $G_1^{[-(1/\rho)(\partial p/\partial s)]'}$ causes downwind advective accelerations, consistent with the structure of $G_1^{(V\partial V/\partial s)'}$. The negative correlation and downwind shift of the downwind turbulent stress divergence relative to downwind pressure gradient above 150 m is consistent with that found by Small et al. (2005) and Song et al. (2006), where SST-induced pressure gradients were seen to drive the turbulent stress divergence response. Contrary to these other studies, this balance does not hold down to the surface in this simulation.

Below 150 m, the SST-induced downwind pressure gradient does not drive the downwind turbulent stress divergence since the first EOFs of the turbulent stress
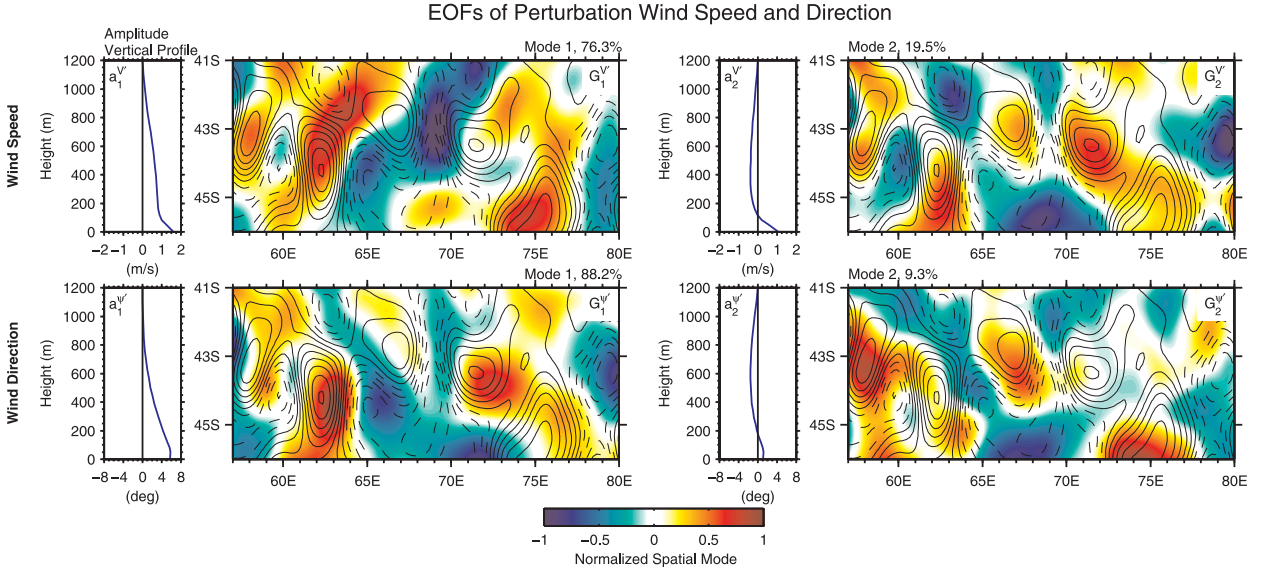
EOFs of Perturbation Wind Speed and Direction

FIG. 9. The first two dominant vertical EOFs of the WRF perturbation (top row) wind speed V' and (bottom row) wind direction ψ'. (left column) The first dominant mode; (right column) the second dominant mode. Within each column, the amplitude vertical profiles are shown at left and maps of the horizontal spatial modes are shown at right. The contours in the maps are of the perturbation AMSR-E SST fields, as shown previously. The percentage of vertical mean product explained by each mode is shown above the maps.

divergence weaken substantially relative to the pressure gradient (Fig. 10). This imbalance is consistent with the intensification of the first EOF of the downwind horizontal advection below 150-m height, as is evident from $a_1^{(V\partial V/\partial s)'}$. Note also the strong similarity between $G_1^{(V\partial V/\partial s)'}$ (Fig. 10) and the surface downwind advection (Fig. 7e). Not only is the difference in vertical structure significant, the downwind lag between the downwind turbulent stress divergence and downwind pressure gradient evident in the first EOFs also contributes strongly to the downwind advective acceleration, since the downwind pressure gradient is unbalanced for ~45 km. The near-surface weakening of the first EOF of the downwind turbulent stress divergence is consistent with stability-dependent turbulent mixing of momentum. For flow from cool to warm SST, enhanced turbulent mixing reduces the drag on the flow below 150 m by mixing momentum from aloft to the surface, thus allowing flow acceleration by the downwind pressure gradient. For flow from warm to cool SST, the turbulent mixing of momentum is reduced, resulting in enhanced drag on the flow below 150 m. Unbalanced pressure-induced accelerations below 150-m height are thus accomplished by changes in near-surface drag made possible by SST-induced modulation of the turbulent mixing of momentum.

The vertical structure of the second EOF mode of the downwind pressure gradient $a_2^{[-(1/\rho)(\partial p/\partial s)]'}$ shows that the pressure gradient changes sign around 200 m above the surface (Fig. 10). From the $G_2^{[-(1/\rho)(\partial p/\partial s)]'}$ fields, the maxima and minima in the spatial pattern of this mode

occur in the transition regions where the downwind SST gradients are largest. Similar changes of sign in the pressure perturbations with height can be seen in simulations over the Gulf Stream by Song et al. (2006) and Wai and Stage (1989), consistent with the vertical structure associated with $a_2^{[-(1/\rho)(\partial p/\partial s)]'}$. In the Wai and Stage (1989) simulation, this structure was seen to be associated with a secondary circulation cell. As we see below, a consequence of the vertical structure of the perturbation pressure gradient field is that the downwind pressure gradient at the surface is not collocated spatially with its vertically averaged counterpart.

We have thus identified physical mechanisms associated with the first two EOF modes of the downwind turbulent stress divergence and the downwind pressure gradient. It is our contention that these two variables explain the horizontal and vertical variability in the first mode EOF of the downwind horizontal advection. This can be tested quantitatively by computing bin averages of $a_1^{(V\partial V/\partial s)'} G_1^{(V\partial V/\partial s)'}$ as a function of $a_1^{(\mathbf{F}\cdot\hat{s})'} G_1^{(\mathbf{F}\cdot\hat{s})'} + a_2^{(\mathbf{F}\cdot\hat{s})'} G_2^{(\mathbf{F}\cdot\hat{s})'} + a_1^{[-(1/\rho)\partial p/\partial s]'} G_1^{[-(1/\rho)\partial p/\partial s]'}$ for all grid points, which is shown in Fig. 11a. The cross correlation between these two fields is 0.81 and there is quite good agreement.

3) WIND DIRECTION AND THE CROSSWIND MOMENTUM BUDGET

The first EOF of the perturbation wind direction ψ' (Fig. 9) shows that the wind rotates clockwise with
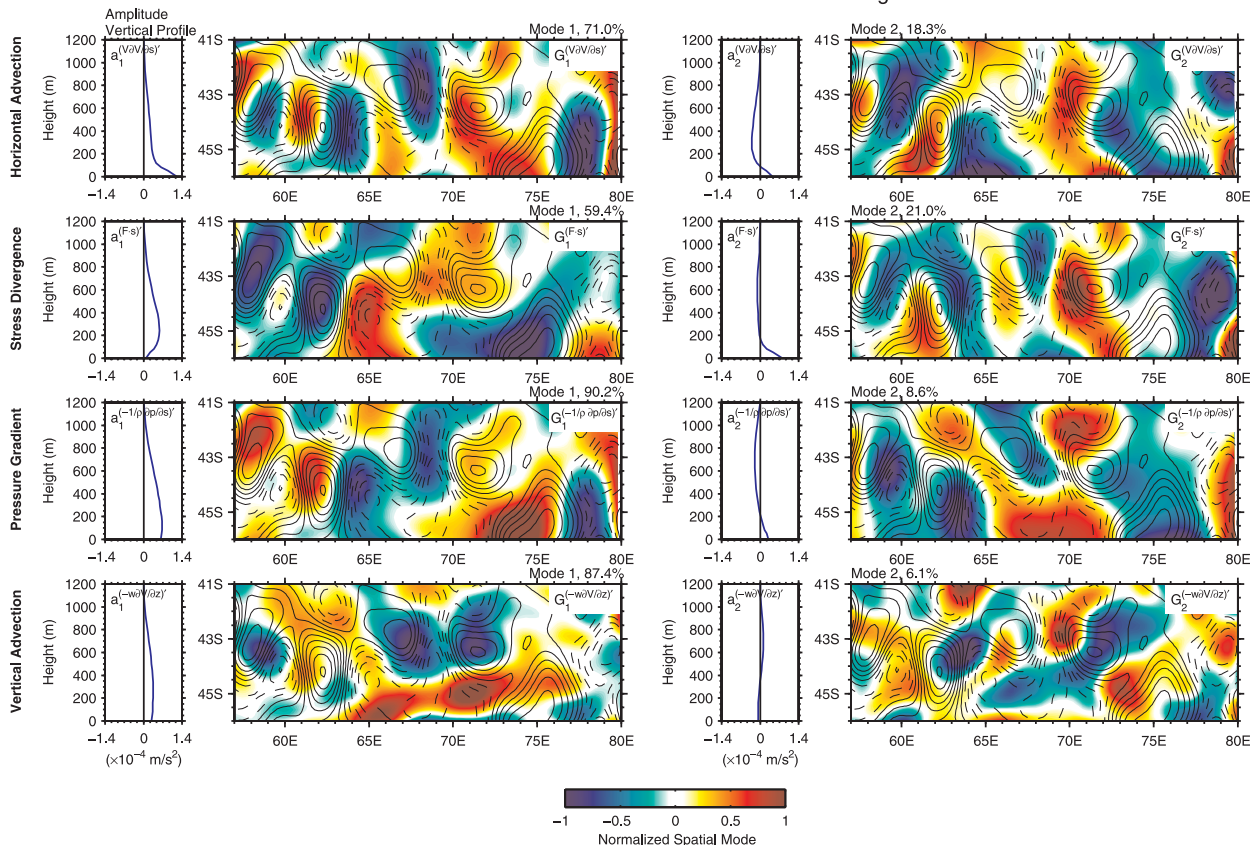
FIG. 10. The first two dominant EOFs of the perturbation terms in the 1-month-averaged WRF downwind momentum budget: (top row) horizontal advection, (second row) turbulent stress divergence, (third row) pressure gradient, and (bottom row) vertical advection. (left column) The first dominant modes; (right column) the second dominant modes. Within each column, the amplitude vertical profiles are shown at left and maps of the horizontal spatial modes are shown at right. The contours in the maps are of the perturbation AMSR-E SST fields, as shown previously. The percentage of vertical mean product explained by each mode is shown above the maps.

height downwind of warm SST perturbations and counterclockwise with height downwind of cool SST perturbations, as is evident qualitatively from Fig. 2b. These wind direction perturbations are largest at the surface and diminish with height. The $G_1^{\psi'}$ field has a maximum cross-correlation coefficient with the perturbation SST of 0.78 when the wind direction perturbations are lagged about 80 km downwind of the SST perturbations and has a very similar pattern to the surface ψ' (Fig. 2d). The second EOF of ψ' has a similar vertical structure as the first EOF, although the horizontal structure is somewhat different; a maximum cross correlation of -0.55 occurs when the $G_2^{\psi'}$ perturbations are lagged about 40 km to the south of the SST perturbations.

EOFs of the crosswind horizontal advection, crosswind turbulent stress divergence, crosswind pressure gradient, Coriolis force, and crosswind vertical advection are shown in Fig. 12. The first EOF of the crosswind pressure gradient explains 97.7% of the vertical variance, diminishes uniformly with height, and has a $G_1^{[-(1/\rho)(\partial p/\partial n)]'}$ field nearly equal to the surface crosswind pressure gradient shown in Fig. 7c. The crosswind pressure gradient is opposed largely by the Coriolis force, as evident by the correspondence between $G_1^{[-(1/\rho)(\partial p/\partial n)]'}$ and $G_1^{(-fV)'}$, although the $G_1^{(-fV)'}$ perturbations are shifted downwind of the $G_1^{[-(1/\rho)(\partial p/\partial n)]'}$ perturbations; the cross-correlation coefficient between these two fields has a minimum of -0.80 when the Coriolis force perturbations are shifted eastward by about 25 km.

Crosswind turbulent stress divergence perturbations contribute to streamline curvature perturbations that are anticyclonic upwind of warm SST and cyclonic upwind of cool SST, as evident from $G_1^{(\mathbf{F}\cdot\hat{n})'}$. They are also strong near the surface, reach a maximum magnitude at about 80-m height, and are relatively small above 600-m height. The second EOFs of the crosswind turbulent stress divergence and Coriolis force have very similar horizontal and vertical structures. The cross correlation
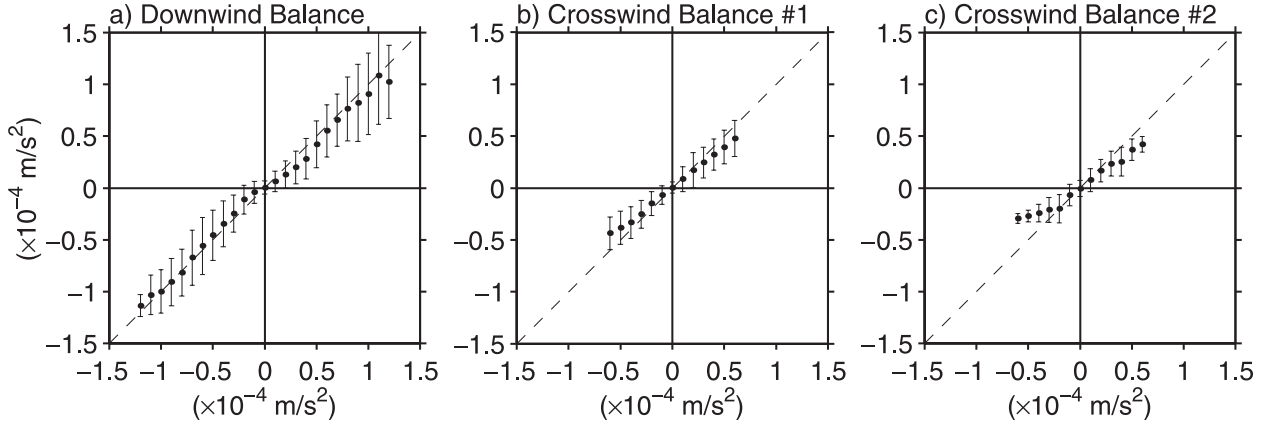
FIG. 11. Binned scatterplots of the dominant balances found from the EOFs in the 1-month-averaged WRF downwind and crosswind momentum budget: (a) downwind balance of $a_1^{(V\partial V/\partial s)'} G_1^{(V\partial V/\partial s)'}$ binned as a function of $a_1^{(\mathbf{F}\cdot\hat{s})'} G_1^{(\mathbf{F}\cdot\hat{s})'} + a_2^{(\mathbf{F}\cdot\hat{s})'} G_2^{(\mathbf{F}\cdot\hat{s})'} + a_1^{[-(1/\rho)(\partial p/\partial s)]'} G_1^{[-(1/\rho)(\partial p/\partial s)]'}$; (b) first crosswind balance of $a_1^{[V^2(\partial\psi/\partial s)(\partial\psi/\partial s)]'} G_1^{(V^2\partial\psi/\partial s)'}$ binned as a function of $a_1^{(\mathbf{F}\cdot\hat{n})'} G_1^{(\mathbf{F}\cdot\hat{n})'} + a_1^{[-(1/\rho)(\partial p/\partial n)]'} G_1^{[-(1/\rho)(\partial p/\partial n)]'} + a_1^{(-fV)'} G_1^{(-fV)'}$; (c) second crosswind balance of $a_2^{(V^2\partial\varphi/\partial s)'} G_2^{(V^2\partial\varphi/\partial s)'}$ binned as a function of $a_2^{(\mathbf{F}\cdot\hat{n})'} \times G_2^{(\mathbf{F}\cdot\hat{n})'} + a_2^{(-fV)'} G_2^{(-fV)'}$. The dashed line in each panel has a slope of 1 and is included for reference. The cross-correlation coefficients for each panel are 0.81, 0.86, and 0.69, respectively.

between $G_2^{(\mathbf{F}\cdot\hat{n})'}$ and $G_2^{(-fV)'}$ is -0.72. Evidently, in flow from warm to cool SST, turbulent mixing decreases rapidly below about 150 m, allowing the unbalanced Coriolis force to turn the winds equatorward. This appears to be consistent with the inertial lee-wave analogy drawn by Spall (2007b).

Two physical mechanisms have thus been identified in the crosswind momentum budget. The first is a balance between the first modes of horizontal advection, pressure gradient, turbulent stress divergence, and the Coriolis force. Quantitative intercomparison of these EOFs is accomplished by bin averaging the first mode crosswind advection $a_1^{(V^2\partial\psi/\partial s)'} G_1^{(V^2\partial\psi/\partial s)'}$ as a function of $a_1^{(\mathbf{F}\cdot\hat{n})'} G_1^{(\mathbf{F}\cdot\hat{n})'} + a_1^{[-(1/\rho)(\partial p/\partial n)]'} G_1^{[-(1/\rho)(\partial p/\partial n)]'} + a_1^{(-fV)'} G_1^{(-fV)'}$ for all grid points (Fig. 11b). The cross correlation of these two quantities is 0.86, and there is good agreement. The second balance drawn here is between the second modes of the horizontal advection, turbulent stress divergence, and the Coriolis force. As before, the second-mode crosswind advection $a_2^{(V^2\partial\psi/\partial s)'} G_2^{(V^2\partial\psi/\partial s)'}$ was binned as a function of $a_2^{(\mathbf{F}\cdot\hat{n})'} G_2^{(\mathbf{F}\cdot\hat{n})'} + a_2^{(-fV)'} G_2^{(-fV)'}$ and is shown in Fig. 11c. The cross correlation is slightly smaller than the others at 0.69, but the spatial patterns of the two fields generally agree well (Fig. 12).

The crosswind vertical shear is to a good approximation in thermal wind balance with the SST-induced air temperature gradients. Qualitatively, cold air advection (i.e., perturbation flow from cool to warm SST) should lead to the perturbation winds turning clockwise with height in the Southern Hemisphere, with the opposite occurring in warm air advection. This can be seen qualitatively in Fig. 2b. This is shown more directly here from comparison of the first and second EOFs of the

crosswind vertical wind shear perturbations $(V\partial\psi/\partial z)'$ and the thermal wind shear components rotated into the crosswind direction, that is, $[(1/\rho f)(\partial/\partial s)(\partial p/\partial z)]'$, which is shown in Fig. 13. These correspond closely, as evident quantitatively from the cross correlation between the first-mode spatial EOFs of the perturbation crosswind vertical wind shear and thermal wind shear components of 0.87. SST-induced baroclinic pressure gradient perturbations thus give rise via the Coriolis force to a vertically sheared turning of the winds. The crosswind turbulent stress component is related to the crosswind vertical shear, and hence the EOF spatial modes of the crosswind turbulent stress are highly correlated with the spatial modes of the crosswind vertical shear (Fig. 13). While the horizontal structures agree very well, the vertical structure differs for two reasons: first, the crosswind turbulent stress component is defined to be zero at the surface in the surface stress boundary condition, and second, the vertical profile of the crosswind turbulent stress also depends on the vertical structure of the eddy viscosity K_M, which tends to be several times larger in the middle of the MABL than near the surface or top (not shown). Crosswind turbulent stress divergence perturbations are therefore consistent with an SST-induced baroclinic modification of the crosswind vertical wind shear.

c. Vertically averaged momentum budgets

From the vertical structure of the downwind turbulent stress divergence in this simulation, it was seen that turbulence redistributes momentum from aloft toward the surface in response to SST-induced surface heating perturbations (Wallace et al. 1989; Hayes et al. 1989)

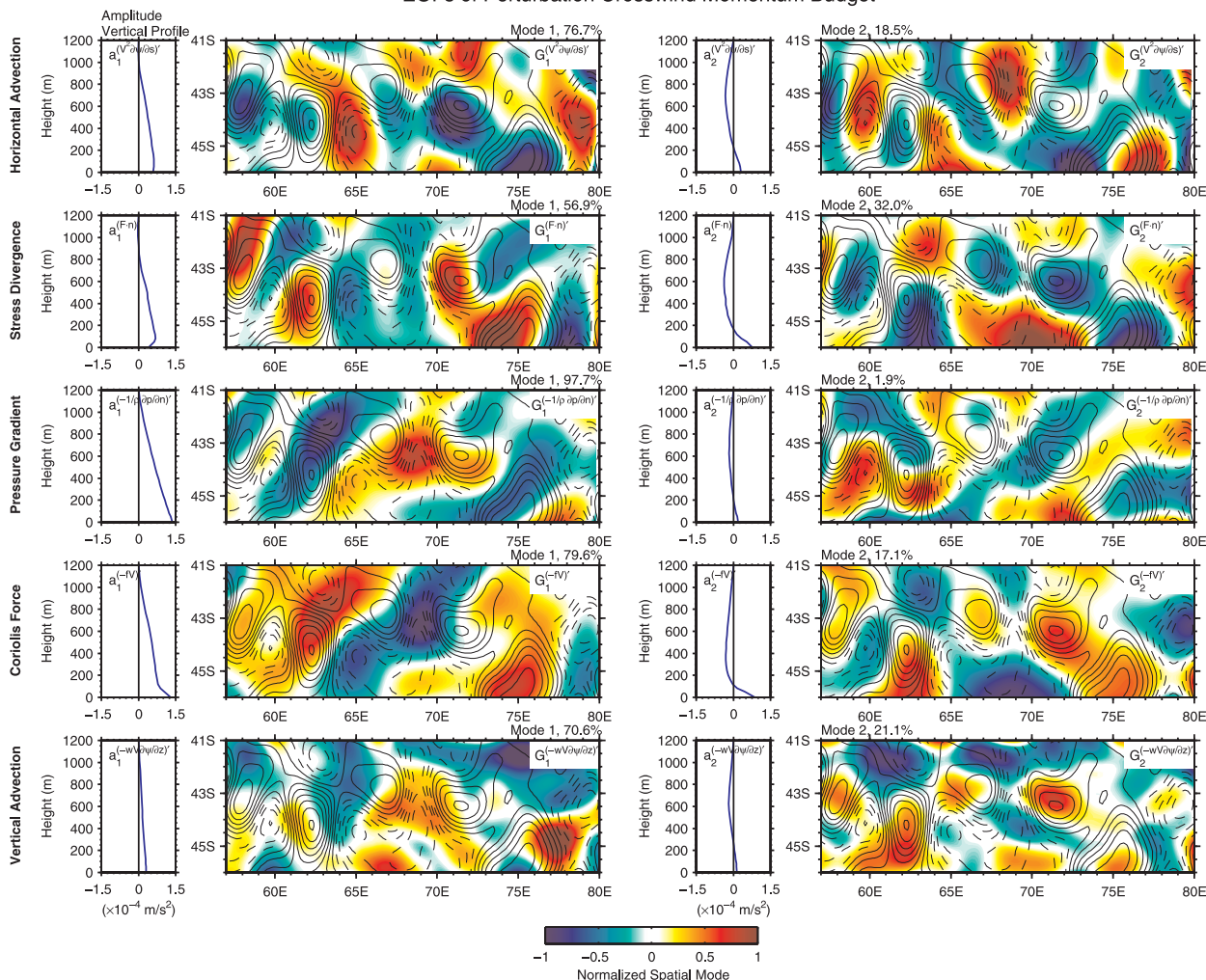EOFs of Perturbation Crosswind Momentum Budget

FIG. 12. The first two dominant EOFs of the perturbation terms in the 1-month-averaged WRF crosswind momentum budget: (top row) horizontal advection, (second row) turbulent stress divergence, (third row) pressure gradient, (fourth row) Coriolis force, and (bottom row) vertical advection. (left column) The first dominant modes; (right column) the second dominant modes. Within each column, the amplitude vertical profiles are shown at left and maps of the horizontal spatial modes are shown at right. The contours in the maps are of the perturbation AMSR-E SST fields, as shown previously. The percentage of vertical mean product explained by each mode is shown above the maps.

below 150 m while also acting as a drag that balances the SST-induced downwind pressure gradients above 150 m (Small et al. 2005). As discussed briefly in the introduction, there is some question about the relationship between the turbulent stress divergence and the surface stress and how the surface stress relates to the other terms in the MABL momentum budget. Part of this concern also involves the relationship between the vertical structure of the forcing terms shown above to the vertically averaged MABL momentum budget.

To explore these relationships, we computed the mass-weighted vertically averaged terms in the momentum budget expressed in Eqs. (3) and (4). The

mass-weighted vertical average is computed from each arbitrary term d in these equations according to

$$\frac{\int_0^{H_B} \rho(z) d(z)\, dz}{\int_0^{H_B} \rho(z)\, dz},$$

where the denominator is the mass per unit area computed at each grid point between the surface and H_B, and then averaged over the 1-month simulation period. The boundary layer depth H_B used for the vertical integration was chosen to be a spatially and temporally
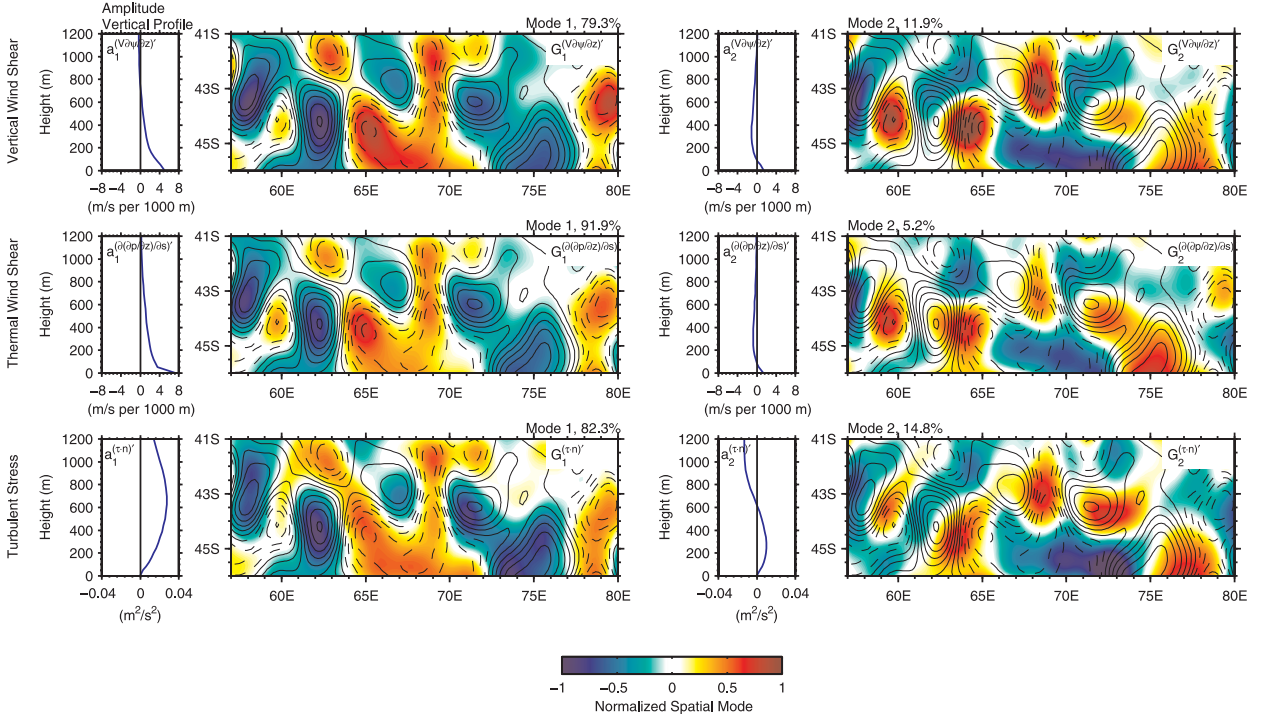
EOFs of Perturbation Crosswind Vertical Shear Terms

FIG. 13. The first two dominant EOFs of the perturbation terms in the 1-month-averaged WRF (top row) crosswind vertical wind shear $(V \partial \psi / \partial z)'$, (middle row) crosswind thermal wind shear $[(1/\rho f)(\partial/\partial s)(\partial p/\partial z)]'$, and (bottom row) the crosswind turbulent stress $\boldsymbol{\tau} \cdot \hat{n}$. (left column) The first dominant mode; (right column) the second dominant mode. Within each column, the amplitude vertical profiles are shown at left and maps of the horizontal spatial mode is shown at right. The contours in the maps are of the 1-month-averaged perturbation AMSR-E SST, as shown previously. The percentage of vertical mean product explained by each mode is shown above the maps.

constant height of 1205 m, which is the height of the twenty-first vertical level of the model grid above the sea surface. A constant height was chosen because, over the model domain, the turbulent stress divergence was roughly an order of magnitude less than its surface value and was nearly zero above this level. Furthermore, SST-induced perturbations in the momentum budget tended to be small above any reasonably defined boundary layer top with little difference between warm and cool SST perturbations. Results based on a spatially and temporally variable MABL depth and entrainment were not qualitatively different from those presented here.

The relationship between the surface stress and the turbulent stress divergence is slightly more complicated in natural coordinates. In the downwind direction,

$$\int_0^{H_B} \mathbf{F} \cdot \hat{s} \, dz = \int_0^{H_B} \left[\frac{\partial (\boldsymbol{\tau} \cdot \hat{s})}{\partial z} - (\boldsymbol{\tau} \cdot \hat{n}) \frac{\partial \psi}{\partial z} \right] dz.$$

The second term on the rhs represents the downwind turbulent stress divergence from the projection of the crosswind stress onto the local streamline in a vertically rotated coordinate system. In this simulation, the cross-

wind turbulent stress $(\boldsymbol{\tau} \cdot \hat{n})$ and $\partial \psi / \partial z$ are small (not shown), so that the second term on the rhs is much smaller than the first term. Thus, the vertically averaged downwind stress divergence is $\int_0^{H_B} \mathbf{F} \cdot \hat{s} \, dz \approx \boldsymbol{\tau} \cdot \hat{s}|_{z=H_B} - \boldsymbol{\tau} \cdot \hat{s}|_{z=0} \approx -\boldsymbol{\tau}_s$, where $\boldsymbol{\tau}_s$, by definition, is computed in the direction of the surface wind in the surface stress boundary condition; that is, $\boldsymbol{\tau}_s = \boldsymbol{\tau} \cdot \hat{s}|_{z=0}$.

Downwind surface stress perturbations correlate very well with the SST perturbations, with a cross-correlation coefficient of -0.89; enhanced stress occurs over warm SST and reduced stress occurs over cool SST (Fig. 14g). These SST-induced surface stress perturbations are opposed largely by the vertically averaged downwind pressure gradient perturbations (Fig. 14h); the correlation coefficient between these fields is -0.76. Differences between the surface stress and vertically averaged downwind pressure gradient give rise to perturbations in the vertically averaged horizontal advection (Fig. 14f).

The vertically averaged downwind momentum budget is much different than the surface downwind momentum budget (Figs. 7e–g). At the surface, downwind turbulent stress divergence and pressure gradient perturbations are

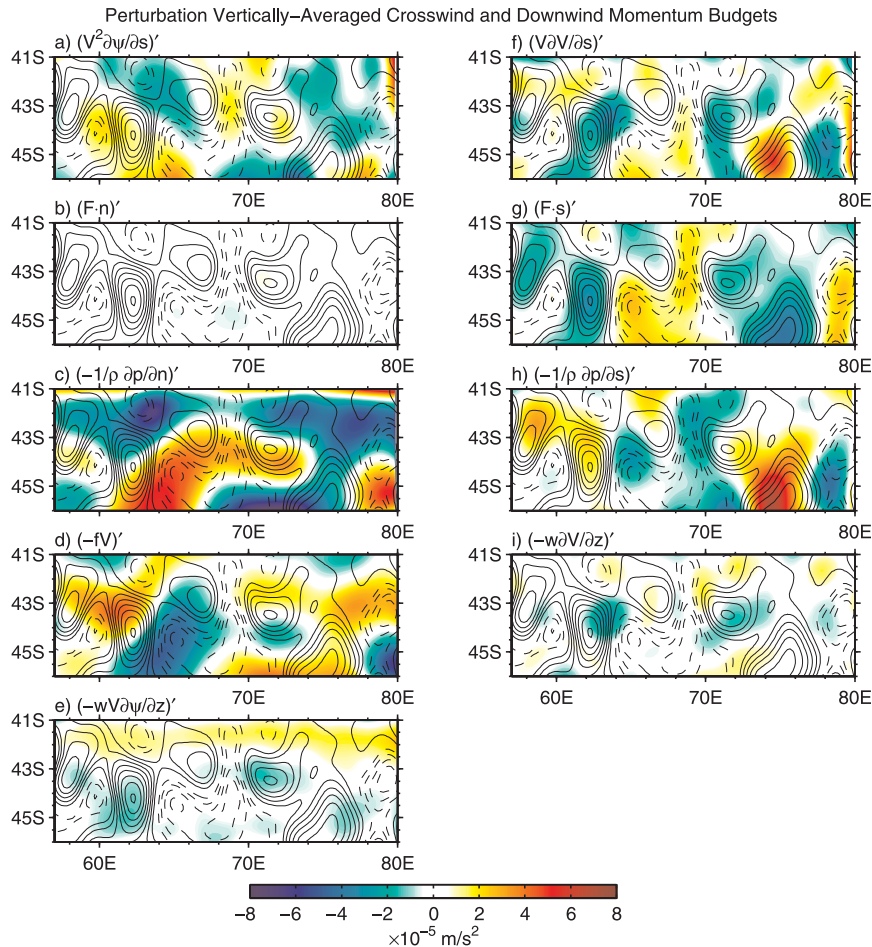Perturbation Vertically–Averaged Crosswind and Downwind Momentum Budgets

FIG. 14. Maps of the terms in the 1-month-averaged WRF perturbation vertically averaged (a)–(e) crosswind momentum budget and (f)–(i) downwind momentum budget. Overlaid in each panel are contours of the perturbation AMSR-E SST, as shown earlier. The vertical averages are mass weighted, as discussed in the text.

collocated with the downwind SST gradients rather than with the SST perturbations themselves as is approximately the case in the vertically averaged downwind stress divergence and downwind pressure gradient. At the surface, the downwind pressure gradient and downwind turbulent stress divergence act together to accelerate the flow, while the surface stress opposes the vertically averaged downwind pressure gradient. This differs from the Small et al. (2005) simulation in which the depth-averaged and surface budgets were comparable in horizontal structure. In this simulation, the vertical structure of the terms in the MABL momentum budget are thus pivotal in describing the complete SST-induced MABL dynamic response in this region; consideration of the vertically averaged MABL momentum budget alone does not adequately describe the surface wind response to mesoscale SST perturbations.

We note that the downwind pressure gradient perturbations at the surface (Fig. 7g) are not collocated with those vertically averaged (Fig. 14h). This is due to the change in sign of the downwind pressure gradient with height seen in the $a_2^{[-(1/\rho)(\partial p/\partial s)]'}$ profile shown in (Fig. 10).

The vertically averaged crosswind turbulent stress divergence is nearly zero, which is expected since the surface crosswind stress is zero by definition in the surface stress boundary condition. Perturbations in the vertically averaged crosswind pressure gradient and Coriolis forces are in an approximate balance (Figs. 14c,d); the correlation coefficient between these two fields is -0.77. The small difference between these two forces is balanced mainly by the perturbation crosswind horizontal advection (Fig. 14a) analogous to a vertically averaged gradient wind balance. Vertical advection is small but

nonnegligible here, but it does not appear related to SST in any clear manner (Fig. 14e).

4. Discussion and conclusions

This study provides the first dynamical analysis of mesoscale wind–SST interactions over the open ocean in the extratropical Southern Hemisphere. We have shown that the high-resolution three-dimensional WRF simulation during the wintertime 1-month period of July 2002 with the Grenier and Bretherton (2001) boundary layer parameterization provides a realistic simulation of the MABL as measured by detailed quantitative comparisons with the QuikSCAT scatterometer surface wind observations.

Several factors contribute to the unique aspects of this simulation. Instead of a single SST front, the meandering Agulhas Return Current produces a quasi-periodic and quasi-stationary series of mesoscale SST perturbations with a spatial scale of $\sim$200 km. This, in addition to the strong surface wind speeds in this region of 10–16 m s^{-1}, results in large surface heat flux differences between warm and cool SST perturbations of 80–100 W m^{-2}. Other characteristics of this simulation include near-neutral stratification of the lower troposphere, the lack of a strong inversion capping the MABL, and little direct influence from landmasses.

Accordingly, the response of the MABL momentum budget to mesoscale SST perturbations in this simulation is found to be distinct from previous numerical simulations in other regions and conditions. Near the surface, the SST-induced downwind pressure gradients and the vertical turbulent momentum redistribution act together to accelerate the surface flow toward warmer water and decelerate the flow toward cooler water. This simulation is the first example of SST-induced surface pressure gradients and turbulent mixing perturbations acting in concert to force surface wind speed perturbations. We may interpret this result as a mixture of the Wallace et al. (1989) and Hayes et al. (1989) turbulent mixing mechanism and the Lindzen and Nigam (1987) and Small et al. (2005) surface pressure gradient forcing mechanism. At the same time, this simulation reproduces the observed result that perturbation surface wind stress maxima are found over warmer water and minima over cooler water. This leads to the counterintuitive result that surface wind stress perturbations and anomalous downwind accelerations of the surface wind due to the turbulent mixing of momentum are not collocated spatially. By vertically averaging the turbulent stress divergence, however, it is shown that the turbulent exchange of horizontal momentum between the lower and upper portions of the MABL driven by SST-induced surface heating perturbations does not make a significant contribution to the surface wind stress in the transition region between warm and cool SST even though it has a significant effect on the surface wind speed.

The SST-induced turbulent stress divergence perturbations thus accomplish two relatively independent tasks in the downwind momentum budget at the mesoscale. The first is exchanging momentum between the lower and upper portions of the MABL, which alters the wind shear in the layer and accelerates or decelerates the surface wind in the transition regions between warm and cool SST but is not collocated with the surface wind stress perturbations. The second is exerting an anomalous surface drag in the vertically averaged downwind momentum budget, which is being driven by anomalous pressure gradient forcing centered over the warm and cool SST perturbations, consistent with the pressure–drag mechanism of Small et al. (2005). As we have noted, the relatively small spatial scale of the SST perturbations and large surface heat flux perturbations in this simulation prevent the MABL from reaching an equilibrium state in which the turbulent wind stress acts as a drag on the SST-induced pressure-driven perturbation flow. Under the nonequilibrium conditions encountered in this simulation, the perturbation surface momentum budget will not necessarily be in qualitative agreement with the vertically averaged momentum budget.

In the crosswind momentum budget, two force balances were identified that lead to wind direction variations associated with the mesoscale SST perturbations. First, crosswind advective accelerations were caused by the imbalance between the SST-induced crosswind pressure gradients, crosswind turbulent stress divergence perturbations, and Coriolis accelerations. Second, a balance between the Coriolis acceleration, crosswind turbulent stress divergence, and crosswind advective accelerations occurred that is analogous to an inertial lee wave driven by modification of the turbulent stress divergence (Spall 2007b). We also showed that the crosswind turbulent stress perturbations were modified by the adjustment of the crosswind vertical wind shear toward a thermal wind balance. The governing crosswind balance is not simply in an inertial flow balance in which the SST-induced wind speed perturbations cause wind direction perturbations via the Coriolis force. Finally, these SST-induced wind direction changes generate significant surface vorticity and divergence perturbations through changes in surface streamline curvature and diffluence in addition to the effects of horizontal wind speed gradients (O'Neill et al. 2010).

REFERENCES

Anderson, S. P., 2001: On the atmospheric boundary layer over the equatorial front. *J. Climate,* **14,** 1688–1695.

Belkin, I. M., and A. L. Gordon, 1996: Southern Ocean fronts from the Greenwich meridian to Tasmania. *J. Geophys. Res.,* **101,** 3675–3696.

Bourras, D., G. Reverdin, H. Giordani, and G. Caniaux, 2004: Response of the atmospheric boundary layer to a mesoscale oceanic eddy in the northeast Atlantic. *J. Geophys. Res.,* **109,** D18114, doi:10.1029/2004JD004799.

Chelton, D. B., and F. J. Wentz, 2005: Global microwave satellite observations of sea surface temperature for numerical weather prediction and climate research. *Bull. Amer. Meteor. Soc.,* **86,** 1097–1115.

——, and Coauthors, 2001: Observations of coupling between surface wind stress and sea surface temperature in the eastern tropical Pacific. *J. Climate,* **14,** 1479–1498.

——, M. G. Schlax, M. H. Freilich, and R. F. Milliff, 2004: Satellite measurements reveal persistent small-scale features in ocean winds. *Science,* **303,** 978–983.

——, ——, and R. M. Samelson, 2007: Summertime coupling between sea surface temperature and wind stress in the California Current System. *J. Phys. Oceanogr.,* **37,** 495–517.

Cronin, M. F., S.-P. Xie, and H. Hashizume, 2003: Barometric pressure variations associated with eastern Pacific tropical instability waves. *J. Climate,* **16,** 3050–3057.

de Szoeke, S. P., and C. S. Bretherton, 2004: Quasi-Lagrangian large eddy simulations of cross-equatorial flow in the east Pacific atmospheric boundary layer. *J. Atmos. Sci.,* **61,** 1837–1858.

Freihe, C. A., and Coauthors, 1991: Air–sea fluxes and surface layer turbulence around a sea surface temperature front. *J. Geophys. Res.,* **96,** 8593–8609.

Gille, S. T., and L. Romero, 2003: Statistical behavior of ALACE floats at the surface of the Southern Ocean. *J. Atmos. Oceanic Technol.,* **20,** 1633–1640.

Grenier, H., and C. S. Bretherton, 2001: A moist PBL parameterization for large-scale models and its application to subtropical cloud-topped marine boundary layers. *Mon. Wea. Rev.,* **129,** 357–377.

Hashizume, H., S.-P. Xie, W. T. Liu, and K. Takeuchi, 2001: Local and remote atmospheric response to tropical instability waves: A global view from space. *J. Geophys. Res.,* **106,** 10 173–10 185.

——, ——, M. Fujiwara, M. Shiotani, T. Watanabe, Y. Tanimoto, W. T. Liu, and K. Takeuchi, 2002: Direct observations of atmospheric boundary layer response to SST variations associated with tropical instability waves over the eastern equatorial Pacific. *J. Climate,* **15,** 3379–3393.

Hayes, S. P., M. J. McPhaden, and J. M. Wallace, 1989: The influence of sea-surface temperature on surface wind in the eastern equatorial Pacific: Weekly to monthly variability. *J. Climate,* **2,** 1500–1506.

Hogg, A. C. M., W. K. Dewar, P. Berloff, S. Kravtsov, and D. K. Hutchinson, 2009: The effects of mesoscale ocean–atmosphere coupling on the large-scale ocean circulation. *J. Climate,* **22,** 4066–4082.

Jin, X., C. Dong, J. Kurian, J. C. McWilliams, and D. B. Chelton, 2009: SST–wind interaction in coastal upwelling: Oceanic simulation with empirical coupling. *J. Phys. Oceanogr.,* **39,** 2957–2970.

Jury, M. R., 1994: Thermal front within the marine atmospheric boundary layer over the Agulhas Current south of Africa: Composite aircraft observations. *J. Geophys. Res.,* **99,** 3297–3304.

——, and N. Walker, 1988: Marine boundary layer modification across the edge of the Agulhas Current. *J. Geophys. Res.,* **93,** 647–654.

Lindzen, R. S., and S. Nigam, 1987: On the role of sea surface temperature gradients in forcing low-level winds and convergence in the tropics. *J. Atmos. Sci.,* **44,** 2418–2436.

Liu, W. T., and W. Tang, 1996: Equivalent neutral wind. JPL publication 96–17, 8 pp.

——, X. Xie, P. S. Polito, S.-P. Xie, and H. Hashizume, 2000: Atmospheric manifestation of tropical instability wave observed by QuikSCAT and tropical rain measuring mission. *Geophys. Res. Lett.,* **27,** 2545–2548.

——, ——, and P. Niiler, 2007: Ocean–atmosphere interaction over Agulhas Extension meanders. *J. Climate,* **20,** 5784–5797.

Lumpkin, R., and M. Pazos, 2007: Measuring surface currents with Surface Velocity Program drifters: The instrument, its data, and some recent results. *Lagrangian Analysis and Prediction of Coastal and Ocean Dynamics,* A. Griffa, et al., Eds., Cambridge University Press, 39–67.

Lutjeharms, J. R. E., 2006: Three decades of research on the greater Agulhas Current. *Ocean Sci. Discuss.,* **3,** 939–995.

——, and I. J. Ansorge, 2001: The Agulhas Return Current. *J. Mar. Syst.,* **30,** 115–138.

Mahrt, L., D. Vickers, and E. Moore, 2004: Flow adjustments across sea-surface temperature changes. *Bound.-Layer Meteor.,* **111,** 553–564.

Milliff, R. F., W. G. Large, W. R. Holland, and J. C. McWilliams, 1996: The general circulation responses of high-resolution North Atlantic Ocean models to synthetic scatterometer winds. *J. Phys. Oceanogr.,* **26,** 1747–1768.

Nonaka, M., and S.-P. Xie, 2003: Covariations of sea surface temperature and wind over the Kuroshio and its extension: Evidence for ocean-to-atmosphere feedback. *J. Climate,* **16,** 1404–1413.

O'Neill, L. W., D. B. Chelton, and S. K. Esbensen, 2003: Observations of SST-induced perturbations on the wind stress field

over the Southern Ocean on seasonal time scales. *J. Climate,* **16,** 2340–2354.

——, ——, ——, and F. J. Wentz, 2005: High-resolution satellite measurements of the atmospheric boundary layer response to SST perturbations over the Agulhas Return Current. *J. Climate,* **18,** 2706–2723.

——, ——, and ——, 2010: The effects of SST-induced horizontal surface wind speed and direction gradients on midlatitude vorticity and divergence. *J. Climate,* **23,** 255–281.

Park, K.-A., and P. C. Cornillon, 2002: Stability-induced modification of sea surface winds over Gulf Stream rings. *Geophys. Res. Lett.,* **29,** 2211, doi:10.1029/2001GL014236.

——, ——, and D. L. Codiga, 2006: Modification of surface winds near ocean fronts: Effects of Gulf Stream rings on scatterometer (QuikSCAT, NSCAT) wind observations. *J. Geophys. Res.,* **111,** C03021, doi:10.1029/2005JC003016.

Rouault, M., and J. R. E. Lutjeharms, 2000: Air–sea exchange over an Agulhas eddy at the subtropical convergence. *Global Atmos. Ocean Syst.,* **7,** 125–150.

Samelson, R. M., E. D. Skyllingstad, D. B. Chelton, S. K. Esbensen, L. W. O'Neill, and N. Thum, 2006: On the coupling of wind stress and sea surface temperature. *J. Climate,* **19,** 1557–1566.

Schlax, M. G., D. B. Chelton, and M. H. Freilich, 2001: Sampling errors in wind fields constructed from single and tandem scatterometer datasets. *J. Atmos. Oceanic Technol.,* **18,** 1014–1036.

Seo, H., A. J. Miller, and J. O. Roads, 2007: The Scripps coupled ocean–atmosphere regional (SCOAR) model, with applications in the eastern Pacific sector. *J. Climate,* **20,** 381–402.

Skamarock, W. C., J. B. Klemp, J. Dudhia, D. O. Gill, D. M. Barker, W. Wang, and J. G. Powers, 2005: A description of the Advanced Research WRF Version 2. NCAR Tech. Note NCAR/TN468+STR, NCAR, 88 pp. [Available online at http://wrf-model.org/wrfadmin/docs/arw_v2.pdf.]

Skyllingstad, E. D., D. Vickers, L. Mahrt, and R. Samelson, 2006: Effects of mesoscale sea-surface temperature fronts on the marine atmospheric boundary layer. *Bound.-Layer Meteor.,* **123,** 219–237, doi:10.1007/s10546-006-9127-8.

Small, R. J., S.-P. Xie, and Y. Wang, 2003: Numerical simulation of atmospheric response to Pacific tropical instability waves. *J. Climate,* **16,** 3722–3740.

——, ——, ——, S. K. Esbensen, and D. Vickers, 2005: Numerical simulation of boundary layer structure and cross-equatorial flow in the eastern Pacific. *J. Atmos. Sci.,* **62,** 1812–1830.

——, and Coauthors, 2008: Air–sea interaction over ocean fronts and eddies. *Dyn. Atmos. Oceans,* **45,** 274–319, doi:10.1016/j.dynatmoce.2008.01.001.

Song, Q., T. Hara, P. Cornillon, and C. A. Friehe, 2004: A comparison between observations and MM5 simulations of the marine atmospheric boundary layer across a temperature front. *J. Atmos. Oceanic Technol.,* **21,** 170–178.

——, P. Cornillon, and T. Hara, 2006: Surface wind response to oceanic fronts. *J. Geophys. Res.,* **111,** C12006, doi:10.1029/2006JC003680.

——, D. B. Chelton, S. K. Esbensen, N. Thum, and L. W. O'Neill, 2009: Coupling between sea surface temperature and low-level winds in mesoscale numerical models. *J. Climate,* **22,** 146–164.

Spall, M. A., 2007a: Effect of sea surface temperature–wind stress coupling on baroclinic instability in the ocean. *J. Phys. Oceanogr.,* **37,** 1092–1097.

——, 2007b: Midlatitude wind stress–sea surface temperature coupling in the vicinity of oceanic fronts. *J. Climate,* **20,** 3785–3801.

Stull, R. B., 1988: *An Introduction to Boundary Layer Meteorology.* Kluwer Academic, 666 pp.

Sweet, W. R., R. Fett, J. Kerling, and P. LaViolette, 1981: Air–sea interaction effects in the lower troposphere across the north wall of the Gulf Stream. *Mon. Wea. Rev.,* **109,** 1042–1052.

Thum, N., 2006: Atmospheric boundary layer coupling to midlatitude mesoscale sea surface temperature anomalies. Ph.D. thesis, Oregon State University, 142 pp. [Available from University Microfilm, 305 N. Zeeb Rd., Ann Arbor, MI 48106.]

Tokinaga, H., Y. Tanimoto, and S.-P. Xie, 2005: SST-induced surface wind variations over the Brazil–Malvinas Confluence: Satellite and in situ observations. *J. Climate,* **18,** 3470–3482.

——, and Coauthors, 2006: Atmospheric sounding over the winter Kuroshio Extension: Effect of surface stability on atmospheric boundary layer structure. *Geophys. Res. Lett.,* **33,** L04703, doi:10.1029/2005GL025102.

Vecchi, G. A., S.-P. Xie, and A. S. Fischer, 2004: Ocean–atmosphere covariability in the western Arabian Sea. *J. Climate,* **17,** 1213–1224.

Wai, M., and S. A. Stage, 1989: Dynamical analysis of marine atmospheric boundary layer structure near the Gulf Stream oceanic front. *Quart. J. Roy. Meteor. Soc.,* **115,** 29–44.

Wallace, J. M., T. P. Mitchell, and C. Deser, 1989: The influence of sea surface temperature on surface wind in the eastern equatorial Pacific: Seasonal and interannual variability. *J. Climate,* **2,** 1492–1499.

Wang, W., D. Barker, C. Bruyere, J. Dudhia, D. Gill, and J. Michalakes, cited 2004: WRF Version 2 modeling system user's guide. [Available online at http://www.mmm.ucar.edu/wrf/users/docs/user_guide_V3/contents.html.]

Warner, T. T., M. N. Lakhtakia, J. D. Doyle, and R. A. Pearson, 1990: Marine atmospheric boundary layer circulations forced by Gulf Stream sea surface temperature gradients. *Mon. Wea. Rev.,* **118,** 309–323.

White, W. B., and J. L. Annis, 2003: Coupling of extratropical mesoscale eddies in the ocean to westerly winds in the atmospheric boundary layer. *J. Phys. Oceanogr.,* **33,** 1095–1107.

Xie, S.-P., 2004: Satellite observations of cool ocean–atmosphere interaction. *Bull. Amer. Meteor. Soc.,* **85,** 195–208.

——, M. Ishiwatari, H. Hashizume, and K. Takeuchi, 1998: Coupled ocean–atmosphere waves on the equatorial front. *Geophys. Res. Lett.,* **25,** 3863–3866.